Abstracta

Ano XXV - N. 06

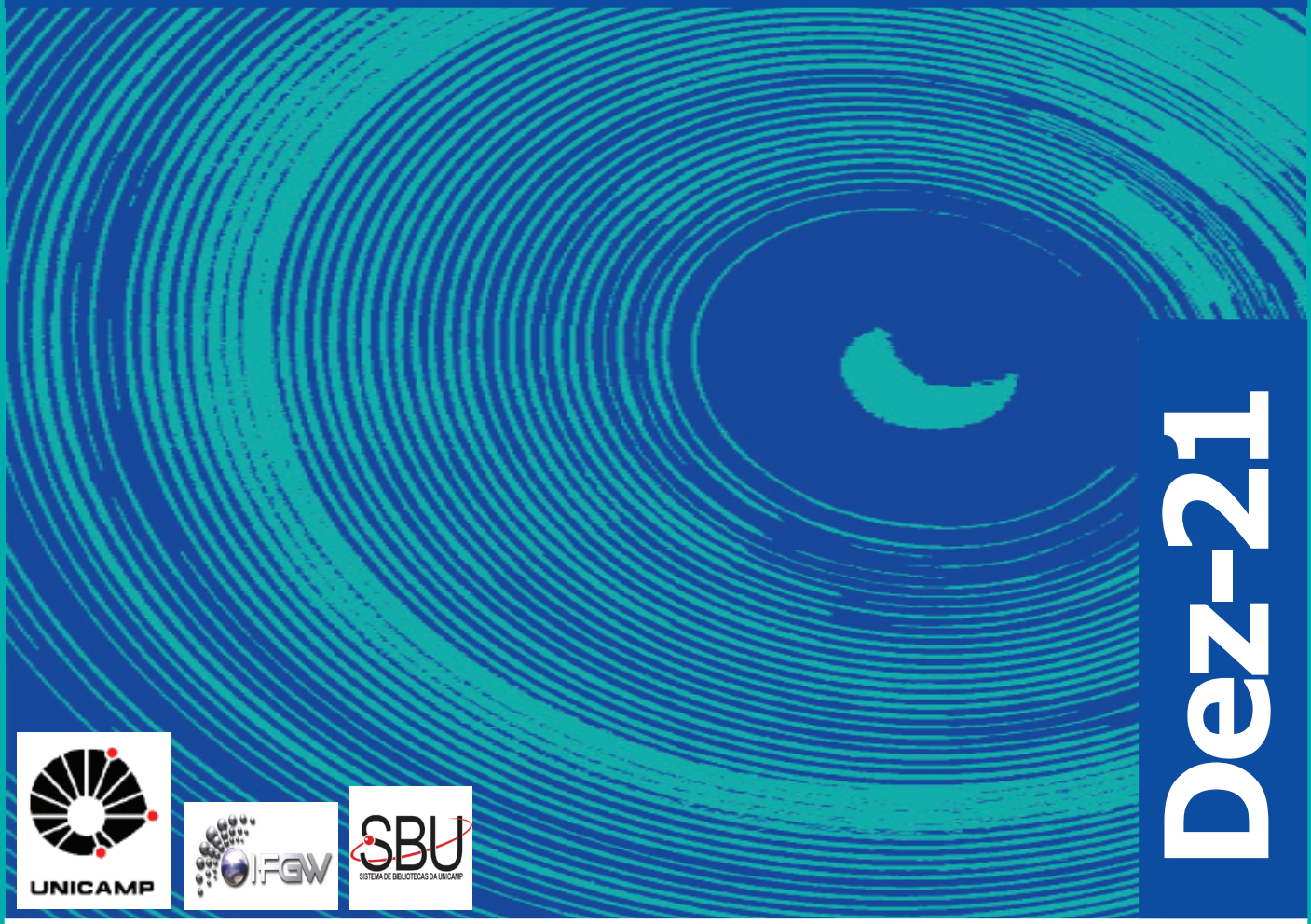

Dez-21

UNICAMP

IFGW

SBU
SISTEMA DE BIBLIOTECAS DA UNICAMP

Artigos publicados
P257-2021 à P327-2021

Correções
Co009-2021

Defesas de Dissertações do IFGW
D020-2021

Defesas de Teses do IFGW
T014-2021

Artigos publicados

[P257-2021] "A Geant4-DNA Evaluation of Radiation-Induced DNA Damage on a Human Fibroblast"

Shin, W. G.; Sakata, D.; Lampe, N.; Belov, O.; Tran, N. H.; Petrovic, I.; Ristic-Fira, A.; Dordevic, M.; **Bernal, M. A.*;** Bordage, M. C.; Francis, Z.; Kyriakou, I.; Perrot, Y.; Sasaki, T.; Villagrasa, C.; Guatelli, S.; Breton, V.; Emfietzoglou, D.; Incerti, S.

Simple Summary: DNA damage caused by ionizing radiation in a human fibroblast cell evaluated by the Geant4-DNA Monte Carlo toolkit is presented. A validation study using a computational geometric human DNA model was then carried out, and the calculated DNA damage as a function of particle type and energy is presented. The results of this work showed a significant improvement on past work and were consistent with recent radiobiological experimental data, such as damage yields. This work and the developed methodology could impact a broad number of research fields in which the understanding of radiation effects is crucial, such as cancer radiotherapy, space science, and medical physics. Abstract: Accurately modeling the radiobiological mechanisms responsible for the induction of DNA damage remains a major scientific challenge, particularly for understanding the effects of low doses of ionizing radiation on living beings, such as the induction of carcinogenesis. A computational approach based on the Monte Carlo technique to simulate track structures in a biological medium is currently the most reliable method for calculating the early effects induced by ionizing radiation on DNA, the primary cellular target of such effects. The Geant4-DNA Monte Carlo toolkit can simulate not only the physical, but also the physico-chemical and chemical stages of water radiolysis. These stages can be combined with simplified geometric models of biological targets, such as DNA, to assess direct and indirect early DNA damage. In this study, DNA damage induced in a human fibroblast cell was evaluated using Geant4-DNA as a function of incident particle type (gammas, protons, and alphas) and energy. The resulting double-strand break yields as a function of linear energy transfer closely reproduced recent experimental data. Other quantities, such as fragment length distribution, scavengeable damage fraction, and time evolution of damage within an analytical repair model also supported the plausibility of predicting DNA damage using Geant4-DNA.The complete simulation chain application "molecularDNA ", an example for users of Geant4-DNA, will soon be distributed through Geant4.

CANCERS 13[19], 4940, 2021. DOI: 10.3390/cancers13194940

[P258-2021] "A polarization from thermalized jet energy"

Serenone, W. M.*; Barbona, J. G. P.*; Chinellato, D. D.;* Lisa, M. A.; Shen, C.; **Takahashi, J.*; Torrieri, G.***

We examine the formation of vortical "smoke rings" as a result of thermalization of energy lost by a jet. We simulate the formation and evolution of these rings using hydrodynamics and define an observable that allows to probe this phenomenon experimentally. We argue that observation of vorticity associated with jets would be an experimental confirmation of the thermalization of the energy lost by quenched jets, and also a probe of shear viscosity.

PHYSICS LETTERS B 820, 136500, 2021. DOI: 10.1016/j.physletb.2021.136500

[P259-2021] "A reactive molecular dynamics study of the hydrogenation of diamond surfaces"

Oliveira, E. F.*; Neupane, M. R.; Li, C. X.; Kannan, H.; Zhang, X.; Puthirath, A. B.; Shah, P. K. B.; Birdwell, A. G.; Ivanov, T. G.; Vajtai, R.; **Galvao, D. S.***; Ajayan, P. M.

Hydrogenated diamond has been regarded as a promising material in electronic device applications, especially in field--effect transistors (FETs). However, the quality of diamond hydrogenation has not yet been established, nor has the specific orientation that would provide the optimum hydrogen coverage. In addition, most theoretical work in the literature use models with 100% hydrogenated diamond surfaces to study electronic properties, which could be unreachable experimentally. In this work, we have carried out a detailed study using fully atomistic reactive molecular dynamics (MD) simulations on low indices diamond surfaces i.e. (001), (013), (1 1 0), (1 1 3), and (1 1 1) to evaluate the quality and hydrogenation thresholds on different diamond surfaces and their possible effects on electronic properties. Our simulation results indicate that the 100% surface hydrogenation on these surfaces is hard to achieve because of the steric repulsion between the terminated hydrogen atoms. Among all the considered surfaces, the (001), (110), and (113) surfaces incorporate a larger number of hydrogen atoms and passivate the surface dangling bonds. Our results on hydrogen stability also suggest that these surfaces with optimum hydrogen coverage are robust under extreme conditions and could provide homogeneous p-type surface conductivity on the diamond surfaces, a key requirement for high-field, high-frequency device applications.

COMPUTATIONAL MATERIALS SCIENCE 200, 110859, 2021. DOI: 10.1016/j.commatsci.2021.110859

[P260-2021] "A(+)c production in pp and in p-Pb collisions at root sNN=5.02 TeV"

Acharya, S.; Adamova, D.; Acharya, S.; Adamova, D.; **Albuquerque, D. S. D.*; Chinellato, D. D.*; Takahashi, J.***; et al. ALICE Collaboration

The production cross section of prompt A(c)(+) charm baryons was measured with the ALICE detector at the LHC at midrapidity in proton-proton (pp) and proton-lead (p-Pb) collisions at a center-of-mass energy per nucleon pair of root sNN = 5.02 TeV. The A(c)(+) and (A) over bar (-)(c)baryons were reconstructed in the hadronic decay channels A(c)(+)-> pK(-)st+ and A(c)(+)-> pK(S)(0) and respective charge conjugates. The measured differential cross sections as a function of transverse momentum (pT) and the pT-integrated A+c production cross section in pp and in p-Pb collisions are presented. The A(c)(+) nuclear modification factor (R-pPb), calculated from the cross sections in pp and in p-Pb collisions, is presented and compared with the R-pPb of D mesons. The A+c /D0 ratio is also presented and compared with the light-flavor baryon-to--meson ratios p/st and A/KS0, and measurements from other LHC experiments. The results are compared to predictions from model calculations and Monte Carlo event generators.

PHYSICAL REVIEW C 104[5], 054905, 2021. DOI: 10.1103/PhysRevC.104.054905

[P261-2021] "Acoustically Driven Stark Effect in Transition Metal Dichalcogenide Monolayers"

Scolfaro, D.*; Finamor, M.*; Trinchao, L. O.*; Rosa, B. L. T.; Chaves, A.; Santos, P. V.; **Iikawa, F.*; Couto Jr., O. D. D.***

The Stark effect is one of the most efficient mechanisms to manipulate many-body states in nanostructured systems. In mono- and few-layer transition metal dichalcogenides, it has been successfully induced by optical and electric field means. Here, we tune the optical emission energies and dissociate excitonic states in MoSe2 monolayers employing the 220 MHz in-plane piezoelectric field carried by surface acoustic waves.

We transfer the monolayers to high dielectric constant piezoelectric substrates, where the neutral exciton binding energy is reduced, allowing us to efficiently quench (above 90%) and red--shift the excitonic optical emissions. A model for the acoustically induced Stark effect yields neutral exciton and trion in--plane polarizabilities of 530 and 630 x 10(-5) meV/(kV/cm)(2), respectively, which are considerably larger than those reported for monolayers encapsulated in hexagonal boron nitride. Large in-plane polarizabilities are an attractive ingredient to manipulate and modulate multiexciton interactions in two-dimensional semiconductor nanostructures for optoelectronic applications.

ACS NANO 15[9], 15371-15380, 2021. DOI: 10.1021/acsnano.1c06854

[P262-2021] "Additively manufactured carbon/black-integrated polylactic acid 3Dprintedsensor for simultaneous quantification of uric acid and zinc in sweat"

Ataide, V. N.; Rocha, D. P.; **Siervo, A. de***; Paixao, T. R. L. C.; Munoz, R. A. A.; Angnes, L.

For the first time the development of an electrochemical method for simultaneous quantification of Zn2+ and uric acid (UA) in sweat is described using an electrochemically treated 3D-printed working electrode. Sweat analysis can provide important information about metabolites that are valuable indicators of biological processes. Improved performance of the 3D-printed electrode was achieved after electrochemical treatment of its surface in an alkaline medium. This treatment promotes the PLA removal (insulating layer) and exposes carbon black (CB) conductive sites. The pH and the square-wave anodic stripping voltammetry technique were carefully adjusted to optimize the method. The peaks for Zn2+ and UA were well-defined at around - 1.1 V and + 0.45 V (vs. CB/PLA pseudo-reference), respectively, using the treated surface under optimized conditions. The calibration curve showed a linear range of 1 to 70 mu g L-1 and 1 to 70 mu mol L-1 for Zn2+ and UA, respectively. Relative standard deviation values were estimated as 4.8% (n = 10, 30 mu g L-1) and 6.1% (n = 10, 30 mu mol L-1) for Zn2+ and UA, respectively. The detection limits for Zn2+ and UA were 0.10 mu g L-1 and 0.28 mu mol L-1, respectively. Both species were determined simultaneously in real sweat samples, and the achieved recovery percentages were between 95 and 106% for Zn2+ and 82 and 108% for UA.

MICROCHIMICA ACTA 188[11], 388, 2021. DOI: 10.1007/s00604-021-05007-5

[P263-2021] "Agarose-Based Fluorescent Waveguide with Embedded Silica Nanoparticle-Carbon Nanodot Hybrids for pH Sensing"

Amato, F.; **Soares, M. C. P.*; Cabral, T. D.***; Fujiwara, E.; **Cordeiro, C. M. D. de B.***; Criado, A.; Prato, M.; Bartoli, J. R.

The fabrication of a biodegradable and fluorescent cylindrical waveguide with doped hybrid nanoparticles (silica-carbon nanodots) is reported. The fluorescent hybrids were obtained by coupling amino-functionalized fumed silica nanoparticles with the carboxylic acid surface groups of amorphous carbon nanodots obtained from the thermolysis of citric acid. The hybrid nanoparticles present diameters lower than 10 nm, maximum fluorescence at 465 nm, and excitation-wavelength-dependent behavior. They were occluded into an agarose matrix, providing a low-cost and easily scalable sensor capable of detecting pH variations with maximum sensitivity of 5.61 nm/(pH unit) when excited by a 403 nm UV light-emitting diode (LED).

ACS APPLIED NANO MATERIALS 4[9], 9738-9751, 2021. DOI: 10.1021/acsanm.1c02127

[P264-2021] "Anisotropic flow of identified hadrons in Xe-Xe collisions at root s(NN)=5.44 TeV"

Acharya, S.; Adamova, D.; **Chinellato, D. D.*; Guardiano, G. G.*; Jahnke, C.*; Takahashi, J.***; et al. ALICE Collaboration

Measurements of elliptic (v(2)) and triangular (v(3)) flow coefficients of pi(+/-), K-+/-, p+(p) over bar, K-S(0), and Lambda+(Lambda) over bar obtained with the scalar product method in Xe-Xe collisions at root sNN = 5.44TeV are presented. The results are obtained in the rapidity range |y| < 0.5 and reported as a function of transverse momentum, p(T), for several collision centrality classes. The flow coefficients exhibit a particle mass dependence for pT < 3 GeV/c, while a grouping according to particle type (i.e., meson and baryon) is found at intermediate transverse momenta (3 < p(T) < 8 GeV/c). The magnitude of the baryon v(2) is larger than that of mesons up to pT = 6 GeV/c. The centrality dependence of the shape evolution of the p(T)-differential v(2) is studied for the various hadron species. The v(2) coefficients of pi(+/-), K-+/-, and p+(p) over bar are reproduced by MUSIC hydrodynamic calculations coupled to a hadronic cascade model (UrQMD) for p(T) < 1 GeV/c. A comparison with vn measurements in the corresponding centrality intervals in Pb-Pb collisions at root sNN = 5.02TeV yields an enhanced v(2) in central collisions and diminished value in semicentral collisions.

JOURNAL OF HIGH ENERGY PHYSICS [10], 152, 2021. DOI: 10.1007/JHEP10(2021)152

[P265-2021] "Antibacterial effect of hyaluronan/chitosan nanofilm in the initial adhesion of Pseudomonas aeruginosa wild type, and IV pili and LPS mutant strains"

Hernandez-Montelongo, J.*; Nicastro, G. G.; Pereira, T. D. O.; **Zavarize, M.***; Beppu, M. M.; Macedo, W. A. A.; Baldini, R. L.; **Cotta, M. A.***

Materials coated with nanofilms obtained by polyelectrolytes assembled layer-by-layer are promising as antibacterial surfaces. Nanofilms of hyaluronan/chitosan (HA/CHI) have satisfactory antibacterial effects against human pathogenic bacteria, such as Escherichia coli and Staphylococcus aureus, but are not efficient for Pseudomonas aeruginosa. To better understand the interaction between P. aeruginosa and HA/CHI nanofilms, this work evaluates the role of type IV pili (T4P) and lipopolysaccharide (LPS) structures in the initial adhesion of this opportunistic pathogen on a bioinert silica substrate and a 20 nm-thick HA/CHI nanofilm using two genetically modified strains: Delta pilA and LPS-. Delta pilA cannot twitch and LPS- lacks the O-antigen structures of LPS molecules. Our results indicate that each strain presented a different adhesion on both surfaces according to their particular features. For the silica substrate, the PA14 wild-type strain exhibited motility because formed interconnected rings, as a result of cell motility; however, in the case of Delta pilA strain, nonconfluent aggregates were generated by the lack of twitching motility in cells. For the LPS- strain, bacteria completely covered the silica, demonstrating a significantly higher rate of adhesion and growth when compared to the other strains. The HA/CHI nanofilm produced membrane damage and lysis on all the used strains, confirming its antibacterial effect during the first hours of culture. However, the lack of LPS seemed to protect the bacteria partially from the HA/CHI nanofilm, probably due to their autoaggregative phenotype, preventing the exposure of part of the cells to the nanofilm. Moreover, in the case of PA14 wild-type, cells were able to adhere on top of the lysed bacteria, using them as a new surface. This behavior may explain why this antibacterial material has not been so efficient against P. aeruginosa for longer culture times.

SURFACES AND INTERFACES 26, 101415, 2021. DOI: 10.1016/j.surfin.2021.101415

[P266-2021] "Application of High-Z Gold Nanoparticles in Targeted Cancer Radiotherapy-Pharmacokinetic Modeling, Monte Carlo Simulation and Radiobiological Effect Modeling"

Li, W. B.; Stangl, S.; Klapproth, A.; Shevtsov, M.; Hernandez, A.; Kimm, M. A.; Schuemann, J.; Qiu, R.; Michalke, B.; **Bernal, M. A.***; Li, J. L.; Huerkamp, K.; Zhang, Y. B.; Multhoff, G.

Simple Summary: High-Z gold nanoparticles show potential as radiosensitizers in the radiotherapy of cancer. In this paper, we introduce the benefits and procedures for the application of gold nanoparticles in targeted cancer radiotherapy. Based on microscopic images of the distribution of antibody-conjugated nanoparticles, we established pharmacokinetic models simulating the biodistribution of nanoparticle conjugates in the tumor and tumor environment in preclinical models. This information has been implemented in radiation transport Monte Carlo simulation codes for further investigating physical and chemical enhancement and radiobiological effects, such as DNA strand breaks and cell survival. Future perspectives and challenges of translating this promising gold nanoparticle-aided radiotherapy into clinical practice are also discussed.</p> High-Z gold nanoparticles (AuNPs) conjugated to a targeting antibody can help to improve tumor control in radiotherapy while simultaneously minimizing radiotoxicity to adjacent healthy tissue. This paper summarizes the main findings of a joint research program which applied AuNP-conjugates in preclinical modeling of radiotherapy at the Klinikum rechts der Isar, Technical University of Munich and Helmholtz Zentrum Munchen. A pharmacokinetic model of superparamagnetic iron oxide nanoparticles was developed in preparation for a model simulating the uptake and distribution of AuNPs in mice. Multi-scale Monte Carlo simulations were performed on a single AuNP and multiple AuNPs in tumor cells at cellular and molecular levels to determine enhancements in the radiation dose and generation of chemical radicals in close proximity to AuNPs. A biologically based mathematical model was developed to predict the biological response of AuNPs in radiation enhancement. Although simulations of a single AuNP demonstrated a clear dose enhancement, simulations relating to the generation of chemical radicals and the induction of DNA strand breaks induced by multiple AuNPs showed only a minor dose enhancement. The differences in the simulated enhancements at molecular and cellular levels indicate that further investigations are necessary to better understand the impact of the physical, chemical, and biological parameters in preclinical experimental settings prior to a translation of these AuNPs models into targeted cancer radiotherapy.

CANCERS 13[21], 5370, 2021. DOI: 10.3390/cancers13215370

[P267-2021] "Cholesterol modulates the interaction between paclitaxel and Langmuir monolayers simulating cell membranes"

Pereira, A. R.; **Shimizu, F. M.***; Oliveira Jr., O. N.

The composition of Langmuir monolayers used as cell membrane models is an essential factor for the interaction with biologically-relevant molecules, including pharmaceutical drugs. In this paper, we report the modulation of effects from the antineoplastic drug paclitaxel by the relative concentration of cholesterol in the Langmuir monolayers of ternary mixtures of dipalmitoylphosphatidylcholine, sphingomyelin, and cholesterol. Since the dependence on cholesterol concentration for these monolayers simulating lipid rafts is non-monotonic, we analyzed the surface pressure and compressibility modulus data with the multidimensional projection technique referred to as interactive document mapping (IDMAP). The maximum expansion induced by paclitaxel in surface pressure isotherms was observed for 27% cholesterol, while the compressibility modulus decreased most strongly for the monolayer with 48% cholesterol. Therefore, the physiological action of paclitaxel may vary depending on whether it is associated with penetration in the membrane or with changes in the membrane elasticity.

COLLOIDS AND SURFACES B-BIOINTERFACES 205, 111889, 2021. DOI: 10.1016/j.colsurfb.2021.111889

[P268-2021] "Combined searches for the production of supersymmetric top quark partners in proton-proton collisions at root s=13 TeV"

Tumasyan, A.; Adam, W.; **Chinellato, J. A.***; et al. CMS Collaboration

A combination of searches for top squark pair production using proton-proton collision data at a center-of-mass energy of 13 TeV at the CERN LHC, corresponding to an integrated luminosity of 137 fb(-1) collected by the CMS experiment, is presented. Signatures with at least 2 jets and large missing transverse momentum are categorized into events with 0, 1, or 2 leptons. New results for regions of parameter space where the kinematical properties of top squark pair production and top quark pair production are very similar are presented. Depending on themodel, the combined result excludes a top squarkmass up to 1325 GeV for amassless neutralino, and a neutralinomass up to 700 GeV for a top squarkmass of 1150 GeV. Top squarks with masses from 145 to 295 GeV, for neutralino masses from 0 to 100 GeV, with a mass difference between the top squark and the neutralino in a window of 30 GeV around the mass of the top quark, are excluded for the first time with CMS data. The results of theses searches are also interpreted in an alternative signal model of dark matter production via a spin-0 mediator in association with a top quark pair. Upper limits are set on the cross section for mediator particle masses of up to 420 GeV.

EUROPEAN PHYSICAL JOURNAL C 81[11], 970, 2021. DOI: 10.1140/epjc/s10052-021-09721-5

[P269-2021] "Constraints on anomalous Higgs boson couplings to vector bosons and fermions in its production and decay using the four-lepton final state"

Tumasyan, A.; Adam, W.; **Chinellato, J. A.***; et al. CMS Collaboration

Studies of CP violation and anomalous couplings of the Higgs boson to vector bosons and fermions are presented. The data were acquired by the CMS experiment at the LHC and correspond to an integrated luminosity of 137 fb(-1) at a proton--proton collision energy of 13 TeV. The kinematic effects in the Higgs boson's four-lepton decay H -> 4l and its production in association with two jets, a vector boson, or top quarks are analyzed, using a full detector simulation and matrix element techniques to identify the production mechanisms and to increase sensitivity to the tensor structure of the Higgs boson interactions. A simultaneous measurement is performed of up to five Higgs boson couplings to electroweak vector bosons (HVV), two couplings to gluons (Hgg), and two couplings to top quarks (Htt). The CP measurement in the Htt interaction is combined with the recent measurement in the H -> gamma gamma channel. The results are presented in the framework of anomalous couplings and are also interpreted in the framework of effective field theory, including the first study of CP properties of the Htt and effective Hgg couplings from a simultaneous analysis of the gluon fusion and top-associated processes. The results are consistent with the standard model of particle physics.

PHYSICAL REVIEW D 104[5], 052004, 2021. DOI: 10.1103/PhysRevD.104.052004

[P270-2021] "Deep-learning based reconstruction of the shower maximum X(max)( )using the water-Cherenkov detectors of the Pierre Auger Observatory"

Aab, A.; Abreu, P.; Aglietta, M.; **Chinellato, J. A.*; Franco, D. D.*; Dobrigkeit, C.*; Fauth, A. C.*; Payeras, A. M.*; Muller, M. A.***; et al. Pierre Auger Collaboration

The atmospheric depth of the air shower maximum X-max is an observable commonly used for the determination of the nuclear mass composition of ultra-high energy cosmic rays. Direct measurements of X-max are performed using observations of the longitudinal shower development with fluorescence telescopes. At the same time, several methods have been proposed for an indirect estimation of X-max from the characteristics of the shower particles registered with surface detector arrays. In this paper, we present a deep neural network (DNN) for the estimation of X-max The reconstruction relies on the signals induced by shower particles in the ground based water-Cherenkov detectors of the Pierre Auger Observatory. The network architecture features recurrent long short-term memory layers to process the temporal structure of signals and hexagonal convolutions to exploit the symmetry of the surface detector array. We evaluate the performance of the network using air showers simulated with three different hadronic interaction models. Thereafter, we account for long--term detector effects and calibrate the reconstructed X-max using fluorescence measurements. Finally, we show that the event-by-event resolution in the reconstruction of the shower maximum improves with increasing shower energy and reaches less than 25 g/cm(2) at energies above 2x10(19) eV.

JOURNAL OF INSTRUMENTATION 16[7], P07019, 2021. DOI: 10.1088/1748-0221/16/07/P07019

[P271-2021] "Didactic laser speckle experiments with a lensless camera"

Fujiwara, E.; Fracarolli, J. A.; **Cordeiro, C. M. B.***

Laser speckles are granular patterns created through the interference of coherent light scattered by a rough surface. Besides comprising an appealing optical phenomenon, the speckle patterns enable applications in physical and biochemical measurements. This paper proposes didactic far-field (objective) speckle experiments using a visible laser source and a lensless webcam for implementation in optics labs or at home. Firstly, a ceramic mug works as the scattering surface to investigate the effect of the target-observation plane distance on the average size of light granules. Secondly, the speckle pattern deviations produced by the liquid inside the recipient are analysed to measure mass and temperature changes. Finally, the mug is replaced with a leaf to evaluate its biological activity based on the scattered light. Image processing tools carry out the quantification of speckle parameters like average size and correlation coefficient, achieving a good agreement between theory and practical results. The proposed far-field speckle experiments explore topics related to optics, instrumentation, and image computing straightforwardly, developing the desired skills for undergraduate and graduate students of physics and engineering courses.

EUROPEAN JOURNAL OF PHYSICS 42[6], 065303, 2021. DOI: 10.1088/1361-6404/ac2b04

[P272-2021] "Effect of Limonene on Modulation of Palm Stearin Crystallization"

Mello, N. A.; **Cardoso, L. P.***; Ribeiro, A. P. B.; Bicas, J. L.

Due to its hard consistency and low plasticity, palm stearin (PS) has limited industrial applications. As described in the literature, the addition of limonene to lipid systems has been shown to influence their crystallization pattern, such as by softening consistency and accelerating polymorphic transition. The objective of this study was to evaluate different concentrations of limonene (1-10%) added to PS, regarding its crystallization behavior. This study reports that limonene addition was able to reduce solid fat content (SFC) and consistency, and delayed crystallization, with more evidenced effects when the highest concentration of limonene was applied (10%). Microstructure and polymorphism were significantly affected by the highest concentrations (7.5% and 10%), tending to the formation of small crystals and their agglomeration, with acceleration of polymorphism. Blending this fat with limonene may broaden its application, considering softer options of PSs.

FOOD BIOPHYSICS 16[1], 1-14, 2021. DOI: 10.1007/s11483-020-09640-0

[P273-2021] "Electron Driven Reactions in Tetrafluoroethane: Positive and Negative Ion Formation"

Pereira-da-Silva, J.; Rodrigues, R.; Ramos, J.; Brigido, C.; Botnari, A.; Silvestre, M.; Ameixa, J.; Mendes, M.; Zappa, F.; Mullock, S. J.; Araujo, J. M. M.; Varella, M. T. D. N.; **Cornetta, L. M.***; Silva, F. F. da

In the search for alternatives to chlorine-containing gases, tetrafluoroethane, CF3CH2F (R134a), a widely used refrigerant gas, has been recognized as a promising substitute for dichlorodifluoromethane, CCl2F2 (R12). When R12 is replaced by R134a, the global warming potential drops from 8100 to 1430, the ozone depletion potential changes from 1 to 0, and the atmospheric lifetime decreases from 100 to 14 years. Electron interactions in the gas phase play a fundamental role in the atmospheric sciences. Here, we present a detailed study on electron-driven fragmentation pathways of CF3CH2F, in which we have investigated processes induced by both electron ionization and electron attachment. The measurements allow us to report the ion efficiency curves for ion formation in the energy range of 0 up to 25 eV. For positive ion formation, R134a dissociates into a wide assortment of ions, in which CF3+ is observed as the most abundant out of seven ions with a relative intensity above 2%. The results are supported by quantum chemical calculations based on bound state techniques, electron-impact ionization models, and electron-molecule scattering simulations, showing a good agreement. Moreover, the experimental first ionization potential was found at 13.10 +/- 0.17 eV and the second at around 14.25 eV. For negative ion formation, C2F3- was detected as the only anion formed, above 8.3 eV. This study demonstrates the role of electrons in the dissociation of R134a, which is relevant for an improvement of the refrigeration processes as well as in atmospheric chemistry and plasma sciences.

JOURNAL OF THE AMERICAN SOCIETY FOR MASS SPECTROMETRY 32[6], 1459-1468, 2021. DOI: 10.1021/jasms.1c00057

[P274-2021] "Emergence of Noncontextuality under Quantum Darwinism"

Baldijao, R. D.*; Wagner, R.; Duarte, C.; Amaral, B.; Cunha, M. T.

Quantum Darwinism proposes that the proliferation of redundant information plays a major role in the emergence of objectivity out of the quantum world. Is this kind of objectivity necessarily classical? We show that if one takes Spekkens's notion of noncontextuality as the notion of classicality and the approach of Brandao, Piani, and Horodecki to quantum Darwinism, the answer to the above question is "'yes," if the environment encodes the proliferated information sufficiently well. Moreover, we propose a threshold on this encoding, above which one can unambiguously say that classical objectivity has emerged under quantum Darwinism.

PRX QUANTUM 2[3], 030351, 2021. DOI: 10.1103/PRXQuantum.2.030351

[P275-2021] "Enhancement of he X-Arapuca photon detection device for he DUNE experiment"

Brizzolari, C.; Brovelli, S.; Bruni, F.; Carniti, P.; Cattadori, C. M.; Falcone, A.; Gotti, C.; **Machado, A. A.***; Meinardi, F.; Pessina, G.; **Segreto, E.***; Souza, H. V.; Spanu, M.; Terranova, F.; Torti, M.

In the Deep Underground Neutrino Experiment (DUNE), the VUV LAr luminescence is collected by light trap devices named X-Arapuca, sizing similar to (480 x 93) mm(2) Six thousand of these units will be deployed in the first DUNE ten kiloton far detector module. In this work we present the first characterisation of the photon detection efficiency of an X-Arapuca device sizing similar to(200 x 75) mm(2) via a complete and accurate set of measurements along the cell longitudinal axis with a movable Am-241 source. The MPPCs photosensors are readout by a cryogenic trans-impedance amplifier to enhance the single photoelectron sensitivity and improve the signal-to-noise while ganging 8 MPPC for a total surface of 288 mm(2) Moreover, we developed a new photon downshifting polymeric material, by which the X-Arapuca photon detection efficiency was enhanced of about +50% with respect to the baseline off-shell product deployed in the standard device configuration. The achieved results are compared to previous measurements on a half size X-Arapuca device, with a fixed source facing the center, with no cold amplification stage, and discussed in view of the DUNE full size optical cell construction for both the horizontal and the vertical drift configurations of the DUNE TPC design and in view of liquid Argon doping by ppms of Xe. Other particle physics projects adopting Liquid Argon as target or active veto, such as Dark Side and LEGEND or the DUNE Near Detector, may take advantage of this novel wavelength shifting material.

JOURNAL OF INSTRUMENTATION 16[9], P09027, 2021. DOI: 10.1088/1748-0221/16/09/P09027

[P276-2021] "Experimental Evidence for an Attractive p-phi Interaction"

Acharya, S.; Adamova, D.; **Chinellato, D. D.*; Guardiano, G. G.*; Jahnke, C.*; Takahashi, J.***; et al. ALICE Collaboration

This Letter presents the first experimental evidence of the attractive strong interaction between a proton and a phi meson. The result is obtained from two-particle correlations of combined p-phi circle plus (p) over bar-phi pairs measured in high--multiplicity pp collisions at root s = 13 TeV by the ALICE Collaboration. The spin-averaged scattering length and effective range of the p-phi interaction are extracted from the fully corrected correlation function employing the Lednicky-Lyuboshits approach. In particular, the imaginary part of the scattering length vanishes within uncertainties, indicating that inelastic processes do not play a prominent role for the p-phi interaction. These data demonstrate that the interaction is dominated by elastic p-phi scattering. Furthermore, an analysis employing phenomenological Gaussian-and Yukawa-type potentials is conducted. Under the assumption of the latter, the N-phi coupling constant is found to be g(N-phi) = 0.14 +/- 0.03(stat) +/- 0.02(syst). This work provides valuable experimental input to accomplish a self-consistent description of the N-phi interaction, which is particularly relevant for the more fundamental studies on partial restoration of chiral symmetry in nuclear medium.

PHYSICAL REVIEW LETTERS 127[17], 172301, 2021. DOI: 10.1103/PhysRevLett.127.172301

[P277-2021] "Extended Navier-Stokes Equations in the Framework of Higher-Order Generalized Hydrodynamics"

Rodrigues, C. G.; **Ramos, J. G.*; Luzzi, R.***; Silva, C. A. B.

In this paper are derived the equations of evolution that govern the hydrodynamic motion of a viscous fluid in nonequilibrium thermodynamic conditions in terms of a basic set of quantities consisting of the density of molecules, the density of energy, and the first and second flux of particle density. For this study was used a higher-order generalized hydrodynamics of order 2 resorting to Heims-Jaynes perturbation expansion for averages retaining only the first-order contribution.

BRAZILIAN JOURNAL OF PHYSICS 51[6], 1904-1915, 2021. DOI: 10.1007/s13538-021-00994-5

[P278-2021] "Extraction of the muon signals recorded with the surface detector of the Pierre Auger Observatory using recurrent neural networks"

Aab, A.; Abreu, P.; Aglietta, M.; **Chinellato, J. A.*; Franco, D. D.*; Dobrigkeit, C.*; Fauth, A. C.*; Payeras, A. M.*; Muller, M. A.***; et al. Pierre Auger Collaboration

The Pierre Auger Observatory, at present the largest cosmic--ray observatory ever built, is instrumented with a ground array of 1600 water-Cherenkov detectors, known as the Surface Detector (SD). The SD samples the secondary particle content (mostly photons, electrons, positrons and muons) of extensive air showers initiated by cosmic rays with energies ranging from 10(17) eV up to more than 10(20) eV. Measuring the independent contribution of the muon component to the total registered signal is crucial to enhance the capability of the Observatory to estimate the mass of the cosmic rays on an event-by-event basis. However, with the current design of the SD, it is difficult to straightforwardly separate the contributions of muons to the SD time traces from those of photons, electrons and positrons. In this paper, we present a method aimed at extracting the muon component of the time traces registered with each individual detector of the SD using Recurrent Neural Networks. We derive the performances of the method by training the neural network on simulations, in which the muon and the electromagnetic components of the traces are known. We conclude this work showing the performance of this method on experimental data of the Pierre Auger Observatory. We find that our predictions agree with the parameterizations obtained by the AGASA collaboration to describe the lateral distributions of the electromagnetic and muonic components of extensive air showers.

JOURNAL OF INSTRUMENTATION 16[7], P07016, 2021. DOI: 10.1088/1748-0221/16/07/P07016

[P279-2021] "Finite-range effects in the unitary Fermi polaron"

Pessoa, R.; **Vitiello, S. A.***; Ardila, L. A. P.

Quantum Monte Carlo techniques are employed to study the properties of polarons in an ultracold Fermi gas, at T = 0, and in the unitary regime using both a zero-range model and a square-well potential. For a fixed density, the potential range is varied and results are extrapolated and compared against a zero-range model. A discussion regarding the choice of an interacting potential with a finite range is presented. We compute the polaron effective mass, the polaron binding energy, and the effective coupling between them. The latter is obtained using the Landau-Pomeranchuk's weakly interacting quasiparticle model. The contact parameter is estimated by fitting the pair distribution function of atoms in different spin states.

PHYSICAL REVIEW A 104[4], 043313, 2021. DOI: 10.1103/PhysRevA.104.043313

[P280-2021] "First measurement of coherent rho(0) photoproduction in ultra-peripheral Xe-Xe collisions at root sNN=5.44 TeV"

Acharya, S.; Adamova, D.; Acharya, S.; Adamova, D.; **Albuquerque, D. S. D.*; Chinellato, D. D.*; Takahashi, J.***; et al. ALICE Collaboration

The first measurement of the coherent photoproduction of rho(0) vector mesons in ultra-peripheral Xe- Xe collisions at root s(NN) = 5.44 TeV is presented. This result, together with previous HERA gamma p data and gamma-Pb measurements from ALICE, describes the atomic number (A) dependence of this process, which is particularly sensitive to nuclear shadowing effects and to the approach to the black-disc limit of QCD at a semi-hard scale. The cross section of the Xe + Xe -> rho(0) + Xe + Xe process, measured at midrapidity through the decay channel rho(0)-> pi(+)pi(-), is found to be d sigma/dy = 131.5 +/- 5.6(stat.)(-16.9)(+17.5) (syst.) mb. The ratio of the continuum to resonant contributions for the production of pion pairs is also measured. In addition, the fraction of events accompanied by electromagnetic dissociation of either one or both colliding nuclei is reported. The dependence on A of cross section for the coherent rho 0 photoproduction at a centre-of-mass energy per nucleon of the gamma A system of W gamma A,n = 65 GeV is found to be consistent with a power--law behaviour sigma (gamma A -> rho(0) A) proportional to A(alpha) with a slope alpha = 0.96 +/- 0.02(syst.). This slope signals important shadowing effects, but it is still far from the behaviour expected in the black-disc limit. (C) 2021 European Organization for Nuclear Research. Published by Elsevier B.V. This is an open access article under the CC BY license (http://creativecommons.org/licenses/by/4.0/). Funded by SCOAP3.

PHYSICS LETTERS B 820, 136481, 2021. DOI: 10.1016/j.physletb.2021.136481

[P281-2021] "First measurement of the cross section for top quark pair production with additional charm jets using dileptonic final states in pp collisions at root s=13 TeV"

Tumasyan, A.; Adam, W.; **Chinellato, J. A.***; et al. CMS Collaboration

The first measurement of the inclusive cross section for top quark pairs (tt) produced in association with two additional charm jets is presented. The analysis uses the dileptonic final states of tt events produced in proton-proton collisions at a centre-of-mass energy of 13 TeV. The data correspond to an integrated luminosity of 41.5 fb-1, recorded by the CMS experiment at the LHC. A new charm jet identification algorithm provides input to a neural network that is trained to distinguish among tt events with two additional charm (ttcc), bottom (ttbb), and light-flavour or gluon (ttLL) jets. By means of a template fitting procedure, the inclusive ttcc, ttbb, and ttLL cross sections are simultaneously measured, together with their ratios to the inclusive tt + two jets cross section. This provides measurements of the ttcc and ttbb cross sections of 10.1 +/- 1.2 (stat) +/- 1.4 (syst) pb and 4.54 +/- 0.35 (stat) +/- 0.56 (syst) pb, respectively, in the full phase space. The results are compared and found to be consistent with predictions from two different matrix element generators with next-to-leading order accuracy in quantum chromodynamics, interfaced with a parton shower simulation.

PHYSICS LETTERS B 820, 136565, 2021. DOI: 10.1016/j.physletb.2021.136565

[P282-2021] "First measurements of N-subjettiness in central Pb-Pb collisions at p root s(NN)=2.76 TeV"

Acharya, S.; Adamova, D.; **Chinellato, D. D.*; Guardiano, G. G.*; Jahnke, C.*; Takahashi, J.***; et al. ALICE Collaboration

The ALICE Collaboration reports the first fully-corrected measurements of the N-subjettiness observable for track-based jets in heavy-ion collisions. This study is performed using data recorded in pp and Pb-Pb collisions at centre-of-mass energies of root s = 7 TeV and root s(NN) = 2.76 TeV, respectively. In particular the ratio of 2-subjettiness to 1-subjettiness, tau(2)/tau(1), which is sensitive to the rate of two-pronged jet substructure, is presented. Energy loss of jets traversing the strongly interacting medium in heavy-ion collisions is expected to change the rate of two-pronged substructure relative to vacuum. The results are presented for jets with a resolution parameter of R = 0.4 and charged jet transverse momentum of 40 <= p(T,jet) <= 60 GeV/c, which constitute a larger jet resolution and lower jet transverse momentum interval than previous measurements in heavy-ion collisions. This has been achieved by utilising a semi-inclusive hadron-jet coincidence technique to suppress the larger jet combinatorial background in this kinematic region. No significant modification of the tau(2)/tau(1) observable for track-based jets in Pb-Pb collisions is observed relative to vacuum PYTHIA6 and PYTHIA8 references at the same collision energy. The measurements of tau(2)/tau(1), together with the splitting aperture angle increment R, are also performed in pp collisions at root s = 7 TeV for inclusive jets. These results are compared with PYTHIA calculations at root s = 7 TeV, in order to validate the model as a vacuum reference for the Pb-Pb centre--of-mass energy. The PYTHIA references for tau(2)/tau(1) are shifted to larger values compared to the measurement in pp collisions. This hints at a reduction in the rate of two--pronged jets in Pb-Pb collisions compared to pp collisions.

JOURNAL OF HIGH ENERGY PHYSICS [10], 3, 2021. DOI: 10.1007/JHEP10(2021)003

[P283-2021] "Flat-band ferromagnetism and spin waves in the Haldane-Hubbard model"

Leite, L. S. G.*; Doretto, R. L.*

We study the flat-band ferromagnetic phase of the Haldane--Hubbard model on a honeycomb lattice within a bosonization scheme for flat-band Chern insulators, focusing on the calculation of the spin-wave excitation spectrum. We consider the Haldane-Hubbard model with the noninteracting lower bands in a nearly flat band limit, previously determined for the spinless model, and at 1/4 filling of its corresponding noninteracting limit. Within the bosonization scheme, the Haldane-Hubbard model is mapped onto an effective interacting boson model, whose quadratic term allows us to determine the spin-wave spectrum at the harmonic approximation. We show that the excitation spectrum has two branches with a Goldstone mode and Dirac points at center and at the K and K' points of the first Brillouin zone, respectively. We also consider the effects on the spin-wave spectrum due to an energy offset in the on--site Hubbard repulsion energies and due to the presence of a staggered on-site energy term, both quantities associated with the two triangular sublattices. In both cases, we find that an energy gap opens at the K and K' points. Moreover, we also find some evidence for an instability of the flat-band ferromagnetic phase in the presence of the staggered on-site energy term. We provide some additional results for the square lattice topological Hubbard model previously studied within the bosonization formalism and comment on the differences between the bosonization scheme implementation for the correlated Chern insulators on both square and honeycomb lattices.

PHYSICAL REVIEW B 104[15], 155129, 2021. DOI: 10.1103/PhysRevB.104.155129

[P284-2021] "Flexure resistant 3D printed zeolite-inspired structures"

Ambekar, R. S.; **Oliveira, E. F.*;** Kushwaha, B.; Pal, V.; Ajayan, P. M.; Roy, A. K.; **Galvao, D. S.***; Tiwary, C. S.

Polymer-based materials exhibit a good combination of strength and ductility but limited flexural strength. Here we demonstrate a family of new zeolite templated interconnected carbon nanotubes like porous networks with unique topologies with enhanced load-bearing and energy-absorbing capabilities. The structures were initially obtained from fully atomistic molecular dynamics simulations and then 3D printed using polylactide serving as an upscaled molecular model. All the structures show multi-fold enhancement in compression and flexural strength as compared to their solid counterparts. The 3D printed structure has 575.41 MPa compressive Young's modulus and 318.87 MPa flexural modulus. The mechanical of the atomic models and 3D printed structures show some scale-independent (in a sense that atomic and macro models show similar behavior) features due to similar topological features and deformation conditions.

ADDITIVE MANUFACTURING 47, 102297, 2021. DOI: 10.1016/j.addma.2021.102297

[P285-2021] "Gain-assisted optical tweezing of plasmonic and large refractive index microspheres"

Ali, R.*; Dutra, R. S.; Pinheiro, F. A.; Neto, P. A. M.

We have theoretically investigated optical tweezing of gain--functionalized microspheres using a highly focused single beam in the nonparaxial regime. We employ the Mie-Debye theory of optical tweezers to calculate the optical force acting on homogeneous and core-shell Mie microspheres with gain. We demonstrate that the optical gain plays a crucial role in optical manipulation, especially to optimize the restoring force and thus allowing for trapping of large refractive index and plasmonic particles. Indeed, we demonstrate that one can trap such particles, which is usually not possible in the case of passive media, by functionalizing them with an optical gain material. We show that by varying the value of the gain, which can be realized by changing the pump power, one can not only achieve trapping but also manipulate the equilibrium position of the tweezed particle. Altogether, our findings open new avenues for gain-assisted optomechanics, where gain functionalized systems could facilitate optical trapping and manipulation of plasmonic nanoparticles in particular, with potential applications in self-assembling of nanoparticle suspensions and on a chip.

JOURNAL OF OPTICS 23[11], 115004, 2021. DOI: 10.1088/2040-8986/ac228f

[P286-2021] "Gas-Phase Fluorination of Hexagonal Boron Nitride"

Meiyazhagan, A.; Serles, P.; Salpekar, D.; **Oliveira, E. F.***; Alemany, L. B.; Fu, R. Q.; Gao, G. H.; Arif, T.; Vajtai, R.; Swaminathan, V.; **Galvao, D. S.***; Khabashesku, V. N.; Filleter, T.; Ajayan, P. M.

Hexagonal boron nitride (hBN) has received much attention in recent years as a 2D dielectric material with potential applications ranging from catalysts to electronics. hBN is a stable covalent compound with a planar hexagonal lattice and is relatively unreactive to most chemical environments, making the chemical functionalization of hBN challenging. Here, a simple, scalable strategy to fluorinate hBN using a direct gas-phase fluorination technique is reported. The nature of fluorine bonding to the hBN lattice and their chemical coordination are described based on various characterization studies and theoretical models. The fluorine functionalized hBN shows a bandgap reduction and displays a semiconducting behavior due to the fluorination process. Additionally, the fluorinated hBN shows significant improvement in its thermal and friction properties, which could be substantial in applications such as lubricants and thermal fluids. Theory and simulations reveal that the enhanced friction properties of fluorinated hBN result from reduced inter-planar interaction energy by electrostatic repulsion of intercalated fluorine atoms between hBN layers without significant disruption of the in-plane lattice. This technique paves the way for the fluorination of several other 2D structures for various applications such as magnetism and functional nanoscale electronic devices.

ADVANCED MATERIALS 2106084, 2021. Early Access Date: OCT. 2021. DOI: 10.1002/adma.202106084

[P287-2021] "Ghost dynamics in the soft gluon limit"

Aguilar, A. C.*; Ambrosio, C. O.*; De Soto, F.; **Ferreira, M. N.*; Oliveira, B. M.***; Papavassiliou, J.; Rodriguez-Quintero, J.

We present a detailed study of the dynamics associated with the ghost sector of quenched QCD in the Landau gauge, where the relevant dynamical equations are supplemented with key inputs originating from large-volume lattice simulations. In particular, we solve the coupled system of Schwinger-Dyson equations that governs the evolution of the ghost dressing function and the ghost-gluon vertex, using as input for the gluon propagator lattice data that have been cured from volume and discretization artifacts. In addition, we explore the soft gluon limit of the same system, employing recent lattice data for the three-gluon vertex that enters in one of the diagrams defining the Schwinger-Dyson equation of the ghost-gluon vertex. The results obtained from the numerical treatment of these equations are in excellent agreement with lattice data for the ghost dressing function, once the latter have undergone the appropriate scale-setting and artifact elimination refinements. Moreover, the coincidence observed between the ghost-gluon vertex in general kinematics and in the soft gluon limit reveals an outstanding consistency of physical concepts and computational schemes.

PHYSICAL REVIEW D 104[5], 054028, 2021. DOI: 10.1103/PhysRevD.104.054028

[P288-2021] "Highly Doped Si Single Crystal Nanowires via Metallic Flux Nanonucleation"

Campanelli, R. B.*; Santos, M. V. P. dos*; Cruz, A. S. E. da*; Pirota, K. R.*; Beron, F.*

Ever since the advent of scalable production of nanodevices, the search for optimal fabrication techniques of low dimensional materials has gained the attention of scientists and engineers all over the world. In particular, the fabrication of silicon nanowires is being increasingly investigated, due to their potential integration into novel technologies such as biological and optical sensors, solar cells, power generators, and transistors, among others. In this context, this work reports the single-step fabrication of Ga-doped Si bulk and nanowire single crystals. They were obtained through the Metallic Flux Nanonucleation (MFNN) technique, where a nanoporous alumina template was employed to define the nanowire morphology, while Ga was used as flux to both lower the Si melting point and dope the crystals. Our results show that Ga-doped silicon bulk crystals were successfully fabricated via MFNN. The carrier concentration was determined by probing the Hall effect and was found to be (2.5 +/- 0.2) x 10(19) cm(-3). Silicon nanowires were simultaneously obtained, presenting an average wire diameter of 125 +/- 26 nm and length up to several tens of microns. These results open the possibility to easily fabricate heavily doped intermetallic cylindrical nanowires, with versatility both on the nanowire composition and the doping element.

IEEE TRANSACTIONS ON NANOTECHNOLOGY 20, 739-743, 2021, DOI: 10.1109/TNANO.2021.3112905

[P289-2021] "Inducing micromechanical motion by optical excitation of a single quantum dot"

Kettler, J.; Vaish, N.; Lepinay, L. M. de; Besga, B.; **Assis, P. L. de***; Bourgeois, O.; Auffeves, A.; Richard, M.; Claudon, J.; Gerard, J. M.; Pigeau, B.; Arcizet, O.; Verlot, P.; Poizat, J. P.

Hybrid quantum optomechanical systems interface a single two-level system with a macroscopic mechanical degree of freedom. In a microwire with a single embedded semiconductor quantum dot, not only can the wire vibration modulate the excitonic transition energy, but the optical drive of the quantum dot can also induce motion in the wire. Hybrid quantum optomechanical systems(1) interface a macroscopic mechanical degree of freedom with a single two-level system such as a single spin(2-4), a superconducting qubit(5-7) or a single optical emitter(8-12). Recently, hybrid systems operating in the microwave domain have witnessed impressive progress(13,14). Concurrently, only a few experimental approaches have successfully addressed hybrid systems in the optical domain, demonstrating that macroscopic motion can modulate the two-level system transition energy(9,10,15). However, the reciprocal effect, corresponding to the backaction of a single quantum system on a macroscopic mechanical resonator, has remained elusive. In contrast to an optical cavity, a two-level system operates with no more than a single energy quantum. Hence, it requires a much stronger hybrid coupling rate compared to cavity optomechanical systems(1,16). Here, we build on the large strain coupling between an oscillating microwire and a single embedded quantum dot(9). We resonantly drive the quantum dot's exciton using a laser modulated at the mechanical frequency. State-dependent strain then results in a time-dependent mechanical force that actuates microwire motion. This force is almost three orders of magnitude larger than the radiation pressure produced by the photon flux interacting with the quantum dot. In principle, the state-dependent force could constitute a strategy to coherently encode the quantum dot quantum state onto a mechanical degree of freedom(1).

NATURE NANOTECHNOLOGY 16[3], 283-+, 2021. DOI: 10.1038/s41565-020-00814-y

[P290-2021] "Intensity of bone involvement: a quantitative F-18-FDG PET/CT evaluation for monitoring outcome of multiple myeloma"

Takahashi, M. E. S.*; Mosci, C.; Duarte, G. O.; Pericole, F. V.; Metze, K.; Lorand-Metze, I. G. H.; Ramos, C. D.

Purpose The parameter intensity of bone involvement (IBI) was recently proposed to quantitatively assess patients with multiple myeloma using F-18-fluorodeoxyglucose-PET combined with computed tomography (F-18-FDG PET/CT) images. Here, we aimed to calculate IBI variation (Delta IBI) between two consecutive PET/CT of the same patient and verified its relationship with a subjective visual analysis of the images and with clinical outcome. Methods Consecutive whole-body F-18-FDG PET/CT performed to assess the outcomes of 29 patients diagnosed with multiple myeloma were retrospectively evaluated. Delta IBI was calculated after bone segmentation, using liver standardized uptake value as a threshold to determine metabolically active volumes in the skeleton. For each pair of consecutive PET/CTs, two nuclear medicine physicians classified visually the most recent image as PET-remission, PET-progression or PET-stable when compared to the previous examination. Results The lowest Delta IBI was -1.27 and the highest was 0.29. PET-remission was related to Delta IBI <0 (median = -0.10; -1.27 to +0.03), while PET-progression was related to Delta IBI >0 (median = 0.02; -0.07 to +0.29). Delta IBI around zero was found in images classified as PET--stable (median = 0.00; -0.08 to +0.06). Significant difference in Delta IBI was found between the three groups. Multivariate stepwise analysis showed that IBI value at diagnostic PET/CT, serum calcium and percentage of plasma cells in the bone marrow are independent prognostic factors. Conclusion Delta IBI provides quantitative data for variations of F-18-FDG uptake in the bone marrow during the follow--up of the patients. In addition, higher IBI values at diagnosis are associated with a higher risk of patient's death.

NUCLEAR MEDICINE COMMUNICATIONS 42[12], 1375-1381, 2021. DOI: 10.1097/MNM.0000000000001470

[P291-2021] "Jet fragmentation transverse momentum distributions in pp and p-Pb collisions at root s, root s(NN)=5.02 TeV"

Acharya, S.; Adamova, D.; Acharya, S.; Adamova, D.; **Albuquerque, D. S. D.*; Chinellato, D. D.*; Takahashi, J.***; et al. ALICE Collaboration

Jet fragmentation transverse momentum (j(T)) distributions are measured in proton-proton (pp) and proton-lead (p-Pb) collisions at root s(NN) = 5.02 TeV with the ALICE experiment at the LHC. Jets are reconstructed with the ALICE tracking detectors and electromagnetic calorimeter using the anti-k(T) algorithm with resolution parameter R = 0.4 in the pseudorapidity range vertical bar eta vertical bar < 0.25. The j(T) values are calculated for charged particles inside a fixed cone with a radius R = 0.4 around the reconstructed jet axis. The measured j(T) distributions are compared with a variety of parton-shower models. Herwig and PYTHIA 8 based models describe the data well for the higher j(T) region, while they underestimate the lower j(T) region. The j(T) distributions are further characterised by fitting them with a function composed of an inverse gamma function for higher j(T) values (called the "wide component"), related to the perturbative component of the fragmentation process, and with a Gaussian for lower j(T) values (called the "narrow component"), predominantly connected to the hadronisation process. The width of the Gaussian has only a weak dependence on jet transverse momentum, while that of the inverse gamma function increases with increasing jet transverse momentum. For the narrow component, the measured trends are successfully described by all models except for Herwig. For the wide component, Herwig and PYTHIA 8 based models slightly underestimate the data for the higher jet transverse momentum region. These measurements set constraints on models of jet fragmentation and hadronisation.

JOURNAL OF HIGH ENERGY PHYSICS [9], 211, 2021. DOI: 10.1007/JHEP09(2021)211

[P292-2021] "K-S(0)- and (anti-)Lambda-hadron correlations in pp collisions at root s=13 TeV"

Acharya, S.; Adamova, D.; **Chinellato, D. D.*; Guardiano, G. G.*; Jahnke, C.*; Takahashi, J.***; et al. ALICE Collaboration

Two-particle Azimuthal correlations are measured with the ALICE apparatus in pp collisions at root s = 13 TeV to explore strangeness- and multiplicity-related effects in the fragmentation of jets and the transition regime between bulk and hard production, probed with the condition that a strange meson (K-S(0)) or baryon (Lambda) with transverse momentum p(T) > 3 GeV/c is produced. Azimuthal correlations between kaons or Lambda hyperons with other hadrons are presented at midrapidity for a broad range of the trigger (3 < p(T)(trigg) < 20 GeV/c) and associated particle p(T) (1 GeV/c < p(T)(assoc) < p(T)(trigg)), for minimum-bias events and as a function of the event multiplicity. The near- and away-side peak yields are compared for the case of either K-S(0) or Lambda((Lambda) over bar)

being the trigger particle with that of inclusive hadrons (a sample dominated by pions). In addition, the measurements are compared with predictions from PYTHIA 8 and EPOS LHC event generators.

EUROPEAN PHYSICAL JOURNAL C 81[10], 945, 2021. DOI: 10.1140/epjc/s10052-021-09678-5

[P293-2021] "Kaon-proton strong interaction at low relative momentum via femtoscopy in Pb-Pb collisions at the LHC"

Acharya, S.; Adamova, D.; Acharya, S.; Adamova, D.; **Albuquerque, D. S. D.*; Chinellato, D. D.*; Takahashi, J.***; et al. ALICE Collaboration

In quantum scattering processes between two particles, aspects characterizing the strong and Coulomb forces can be observed in kinematic distributions of the particle pairs. The sensitivity to the interaction potential reaches a maximum at low relative momentum and vanishing distance between the two particles. Ultrarelativistic heavy-ion collisions at the LHC provide an abundant source of many hadron species and can be employed as a measurement method of scattering parameters that is complementary to scattering experiments. This study confirms that momentum correlations of particles produced in Pb-Pb collisions at the LHC provide an accurate measurement of kaon-proton scattering parameters at low relative momentum, allowing precise access to the K- p -> K- p process. This work also validates the femtoscopic measurement in ultrarelativistic heavy-ion collisions as an alternative to scattering experiments and a complementary tool to the study of exotic atoms with comparable precision. In this work, the first femtoscopic measurement of momentum correlations of K- p (K+(p) over bar) and K+p (K-(p) over bar) pairs in Pb-Pb collisions at centre-of-mass energy per nucleon pair of root sNN = 5.02 TeV registered by the ALICE experiment is reported. The components of the K- p complex scattering length are extracted and found to be Rf(0) = -0.91 +/- 0.03(stat)(-0.03)(+0.17) (syst) and Sf(0) = 0.92 +/- 0.05(stat)(-0.33)(+0.12)(syst). The results are compared with chiral effective field theory predictions as well as with existing data from dedicated scattering and exotic kaonic atom experiments.

PHYSICS LETTERS B 822, 136708, 2021. DOI: 10.1016/j.physletb.2021.136708

[P294-2021] "Long- and short-range correlations and their event-scale dependence in high-multiplicity pp collisions at s=13 TeV"

Acharya, S.; Adamova, D.; Acharya, S.; Adamova, D.; **Albuquerque, D. S. D.*; Chinellato, D. D.*; Takahashi, J.*;** et al. ALICE Collaboration

Two-particle angular correlations are measured in high-multiplicity proton-proton collisions at = 13 TeV by the ALICE Collaboration. The yields of particle pairs at short-(eta similar to 0) and long-range (1.6 < |<eta>| < 1.8) in pseudorapidity are extracted on the near-side (<similar to> 0). They are reported as a function of transverse momentum (p(T)) in the range 1 < p(T)< 4 GeV/c. Furthermore, the event-scale dependence is studied for the first time by requiring the presence of high--p(T) leading particles or jets for varying p(T) thresholds. The results demonstrate that the long-range "ridge" yield, possibly related to the collective behavior of the system, is present in events with high-p(T) processes as well. The magnitudes of the short- and long-range yields are found to grow with the event scale. The results are compared to EPOS LHC and PYTHIA 8 calculations, with and without string-shoving interactions. It is found that while both models describe the qualitative trends in the data, calculations from EPOS LHC show a better quantitative agreement for the p(T) dependency, while overestimating the event-scale dependency.

JOURNAL OF HIGH ENERGY PHYSICS [5], 290, 2021. DOI: 10.1007/JHEP05(2021)290

[P295-2021] "Measurement of the electroweak production of Z gamma and two jets in proton-proton collisions at root s=13 TeV and constraints on anomalous quartic gauge couplings"

Tumasyan, A.; Adam, W.; **Chinellato, J. A.***; et al. CMS Collaboration

The first observation of the electroweak (EW) production of a Z boson, a photon, and two forward jets (Z gamma jj) in proton-proton collisions at a center-of-mass energy of 13 TeV is presented. A data set corresponding to an integrated luminosity of 137 fb(-1), collected by the CMS experiment at the LHC in 2016-2018 is used. The measured fiducial cross section for EW Z gamma jj is sigma(Ew)= 5.21 +/- 0.52(stat)+/- 0.56(syst) fb = 5.21 +/- 0.76 fb. Single-differential cross sections in photon, leading lepton, and leading jet transverse momenta, and double-differential cross sections in mjj and vertical bar Delta eta(jj)vertical bar are also measured. Exclusion limits on anomalous quartic gauge couplings are derived at 95% confidence level in terms of the effective field theory operators M-0 to M-5, M-7, T-0 to T-2, and T-5 to T-9.

PHYSICAL REVIEW D 104[7], 072001, 2021. DOI: 10.1103/PhysRevD.104.072001

[P296-2021] "Measurement of the production cross section of prompt Xi(0)(c) baryons at midrapidity in pp collisions at root s=5.02 TeV"

Acharya, S.; Adamova, D.; **Chinellato, D. D.*; Guardiano, G. G.*; Jahnke, C.*; Takahashi, J.***; et al. ALICE Collaboration

The transverse momentum (p(T)) differential cross section of the charm-strange baryon Xi(0)(c) is measured at midrapidity (vertical bar y vertical bar < 0.5) via its semileptonic decay into e(+)Xi(-)nu(e) in pp collisions at root s = 5.02TeV with the ALICE detector at the LHC. The ratio of the p(T)-differential Xi(0)(c)--baryon and D-0-meson production cross sections is also reported. The measurements are compared with simulations with different tunes of the PYTHIA 8 event generator, with predictions from a statistical hadronisation model (SHM) with a largely augmented set of charm-baryon states beyond the current lists of the Particle Data Group, and with models including hadronisation via quark coalescence. The pT-integrated cross section of prompt Xi(0)(c)-baryon production at midrapidity is also reported, which is used to calculate the baryon-to-meson ratio Xi(0)(c)/D-0 = 0.20 +/- 0.04 (stat.)(-0.07)(+0.08) (syst.). These results provide an additional indication of a modification of the charm fragmentation from e(+) e(-) and e-p collisions to pp collisions.

JOURNAL OF HIGH ENERGY PHYSICS [10], 159, 2021. DOI: 10.1007/JHEP10(2021)159

[P297-2021] "Measurements of the pp -> W-+/-gamma gamma and pp -> Z gamma gamma cross sections at root s=13 TeV and limits on anomalous quartic gauge couplings"

Tumasyan, A.; Adam, W.; **Chinellato, J. A.***; et al. CMS Collaboration

The cross section for W or Z boson production in association with two photons is measured in proton-proton collisions at a centre--of-mass energy of 13 TeV. The data set corresponds to an integrated luminosity of 137 fb(-1) collected by the CMS experiment at the LHC. The W -> l nu and Z -> ll decay modes (where l = e, mu) are used to extract the W gamma gamma and Z gamma gamma cross sections in a phase space defined by electron (muon)

with transverse momentum larger than 30 GeV and photon transverse momentum larger than 20 GeV. All leptons and photons are required to have absolute pseudorapidity smaller than 2.5. The measured cross sections in this phase space are sigma(W gamma gamma) = 13.6(-1.9)(+1.9) (stat)(-4.0)(+4.0) (syst) +/- 0.08 (PDF + scale) fb and sigma(Z gamma gamma) = 5.41(-0.55)(+0.58) (stat)(-0.70)(+0.64) (syst) +/- 0.06 (PDF + scale) fb. Limits on anomalous quartic gauge couplings are set in the framework of an effective field theory with dimension-8 operators.

JOURNAL OF HIGH ENERGY PHYSICS [10], 174, 2021. DOI: 10.1007/JHEP10(2021)174

[P298-2021] "Microscopic origin of the high thermoelectric figure of merit of n-doped SnSe"

Chaves, A. S.*; Larson, D. T.; Kaxiras, E.; **Antonelli, A.***

Excellent thermoelectric performance in the out-of-layer n--doped SnSe has been observed experimentally [Chang et al., 160. 778 (2018)]. However, a first-principles investigation of the dominant scattering mechanisms governing all thermoelectric transport properties is lacking. In the present paper, by applying extensive first-principles calculations of electron-phonon coupling associated with parameterized calculation of the scattering by ionized impurities, we investigate the reasons behind the superior figure of merit as well as the enhancement of zT above 600 K in n-doped out-of-layer SnSe, as compared to p-doped SnSe with similar carrier densities. For the n-doped case, the relaxation time is dominated by ionized impurity scattering and increases with temperature, a feature that maintains the power factor at high values at higher temperatures and simultaneously causes the carrier thermal conductivity at zero electric current (k(e1)) to decrease faster for higher temperatures, leading to an ultrahigh-zT = 3.1 at 807 K. We rationalize the roles played by k(el) and K-0 (the thermal conductivity due to carrier transport under isoelectrochemical conditions) in the determination of zT. Our results show the ratio between K-0 and the lattice thermal conductivity indeed corresponds to the upper limit for zT, whereas the difference between calculated zT and the upper limit is proportional to K-e1.

PHYSICAL REVIEW B 104[11], 115204, 2021. DOI: 10.1103/PhysRevB.104.115204

[P299-2021] "Neutrino primordial Planckian black holes"

Carneiro, S.; **Holanda, P. C. de***; Saa, A.

Extremal rotating black holes can be formed in the Planck energy scattering of Dirac spin parallel neutrinos in the mass state m(2) (assuming m(1) = 0), owing to the repulsive interaction between their magnetic dipoles, induced by vacuum fluctuations. Assuming that some recent results of loop--quantised Schwarzschild black holes would be also applicable for the Kerr case, we show that the resulting black hole has Planck mass and angular momentum h over line , and that its horizon area is in the spectrum of the Loop Quantum Gravity area operator. Moreover, we argue that such black holes could be produced at the reheating, with an abundance that allows their interpretation as forming the presently observed dark matter component, provided that the energy scale at inflation is approximate to 10(17) GeV. This scale can be lower if we attribute a high chemical potential to primordial neutrinos. As extremal black holes have zero surface gravity, there is no limits on their abundance from Hawking evaporation.

PHYSICS LETTERS B 822, 136670, 2021. DOI: 10.1016/j.physletb.2021.136670

[P300-2021] "Observation of Forward Neutron Multiplicity Dependence of Dimuon Acoplanarity in Ultraperipheral Pb--Pb Collisions at root S-NN=5.02 TeV"

Tumasyan, A.; Adam, W.; **Chinellato, J. A.***; et al. CMS Collaboration

The first measurement of the dependence of gamma gamma -> mu(+)mu(-) production on the multiplicity of neutrons emitted very close to the beam direction in ultraperipheral heavy ion collisions is reported. Data for lead-lead interactions at root S-NN = 5.02 TeV, with an integrated luminosity of approximately 1.5 nb(-1), are collected using the CMS detector at the LHC. The azimuthal correlations between the two muons in the invariant mass region 8 < m(mu mu) < 60 GeV are extracted for events including 0, 1, or at least 2 neutrons detected in the forward pseudorapidity range vertical bar eta vertical bar > 8.3. The back-to-back correlation structure from leading--order photon-photon scattering is found to be significantly broader for events with a larger number of emitted neutrons from each nucleus, corresponding to interactions with a smaller impact parameter. This observation provides a data-driven demonstration that the average transverse momentum of photons emitted from relativistic heavy ions has an impact parameter dependence. These results provide new constraints on models of photon-induced interactions in ultraperipheral collisions. They also provide a baseline to search for possible final-state effects on lepton pairs caused by traversing a quark-gluon plasma produced in hadronic heavy ion collisions.

PHYSICAL REVIEW LETTERS 127[12], 122001, 2021. DOI: 10.1103/PhysRevLett.127.122001

[P301-2021] "On the relationship between the Raman scattering features and the Ti-related chemical states of TixOyNz films"

Zanatta, A. R.; **Cemin, F.*; Echeverrigaray, F. G.*; Alvarez, F.***

Owing to its singular and (to some extend) adaptable characteristics, titanium oxynitride (TixOyNz) represents an exceptional choice in the realm of new materials aiming at the development of practical devices. However, the effective use of TixOyNz in photovoltaic and (photo)catalysis applications, for example, relies on a refined production-properties balance. Accordingly, this paper reports on the physico-chemical properties of TixOyNz films as investigated by means of the Raman scattering and X-ray photoelectron spectroscopy (XPS) techniques - the former shedding light on the structural characteristics of the films, and the latter providing the state of oxidation of the film's constituents. The films were prepared by sputtering TiO2 and Ti targets in a plasma comprising different mixtures of Ar and N-2. Because of the deposition method and conditions, the films exhibit Raman spectra that are consistent with a combination of TiO2 and TiN or, more properly, TixOyNz under the amorphous and (nano/micro-)crystalline structures. In fact, the experimental data indicate the presence of four TiO2- and two TiN-related phonon modes, whose relative scattering features scale with the oxygen and nitrogen contents of the films. A similar concentration dependence was verified with the percentage of Ti4+, Ti3+, and Ti2+ chemical states of oxidation. This mutual concentration dependence was explored thoroughly and the results clearly indicate the suitability of the Raman data to estimate the typical atom composition and distribution of the Ti-related chemical states of TixOyNz. (

JOURNAL OF MATERIALS RESEARCH AND TECHNOLOGY--JMR&T 14, 864-870, 2021. DOI: 10.1016/j.jmrt.2021.06.090

[P302-2021] "Optomechanical quantum teleportation"

Fiaschi, N.; Hensen, B.; Wallucks, A.; **Benevides, R.*;** Li, J.; **Alegre, T. P. M.***; Groblacher, S.

Quantum teleportation, the faithful transfer of an unknown input state onto a remote quantum system(1), is a key component in long-distance quantum communication protocols(2) and distributed quantum computing(3,4). At the same time, high-frequency nano-optomechanical systems(5) hold great promise as nodes in a future quantum network(6), operating on-chip at low-loss optical telecom wavelengths with long mechanical lifetimes. Recent demonstrations include entanglement between two resonators(7), a quantum memory(8) and microwave-to-optics transduction(9-11). Despite these successes, quantum teleportation of an optical input state onto a long-lived optomechanical memory is an outstanding challenge. Here we demonstrate quantum teleportation of a polarization-encoded optical input state onto the joint state of a pair of nanomechanical resonators. Our protocol also allows to store and retrieve an arbitrary qubit state onto a dual-rail encoded optomechanical quantum memory. This work demonstrates the full functionality of a single quantum repeater node and presents a key milestone towards applications of optomechanical systems as quantum network nodes.

NATURE PHOTONICS 15[11], 817-+, 2021. DOI: 10.1038/s41566-021-00866-z

[P303-2021] "Optomechanical synchronization across multi-octave frequency spans"

Rodrigues, C. C.*; Kersul, C. M.*; Primo, A. G.*; Lipson, M.; **Alegre, T. P. M.*; Wiederhecker, G. S.***

Experimental exploration of synchronization in scalable oscillator microsystems has unfolded a deeper understanding of networks, collective phenomena, and signal processing. Cavity optomechanical devices have played an important role in this scenario, with the perspective of bridging optical and radio frequencies through nonlinear classical and quantum synchronization concepts. In its simplest form, synchronization occurs when an oscillator is entrained by a signal with frequency nearby the oscillator's tone, and becomes increasingly challenging as their frequency detuning increases. Here, we experimentally demonstrate entrainment of a silicon-nitride optomechanical oscillator driven up to the fourth harmonic of its 32 MHz fundamental frequency. Exploring this effect, we also experimentally demonstrate a purely optomechanical RF frequency divider, where we performed frequency division up to a 4:1 ratio, i.e., from 128 MHz to 32 MHz. Further developments could harness these effects towards frequency synthesizers, phase-sensitive amplification and nonlinear sensing. Higher order synchronization in optomechanical devices is relatively unexplored. Here the authors use nonlinear parametric effects to entrain an optomechanical oscillator with a drive signal several octaves away from the oscillation frequency, and demonstrate RF frequency division.

NATURE COMMUNICATIONS 12[1], 5625, 2021. DOI: 10.1038/s41467-021-25884-x

[P304-2021] "Ott-Antonsen ansatz for the D-dimensional Kuramoto model: A constructive approach"

Barioni, A. E. D.*; Aguiar, M. A. M. de*

Kuramoto's original model describes the dynamics and synchronization behavior of a set of interacting oscillators represented by their phases. The system can also be pictured as a set of particles moving on a circle in two dimensions, which allows a direct generalization to particles moving on the surface of higher dimensional spheres. One of the key features of the 2D system is the presence of a continuous phase transition to synchronization as the coupling intensity increases. Ott and Antonsen proposed an ansatz for the distribution of oscillators that allowed them to describe the dynamics of the order parameter with a single differential equation. A similar ansatz was later proposed for the D-dimensional model by using the same functional form of the 2D ansatz and adjusting its parameters. In this article, we develop a constructive method to find the ansatz, similarly to the procedure used in 2D. The method is based on our previous work for the 3D Kuramoto model where the ansatz was constructed using the spherical harmonics decomposition of the distribution function. In the case of motion in a D-dimensional sphere, the ansatz is based on the hyperspherical harmonics decomposition. Our result differs from the previously proposed ansatz and provides a simpler and more direct connection between the order parameter and the ansatz.

CHAOS 31[11], 113141, 2021. DOI: 10.1063/5.0069350

[P305-2021] "Peripheral microcirculatory alterations are associated with the severity of acute respiratory distress syndrome in COVID-19 patients admitted to intermediate respiratory and intensive care units"

Mesquida, J.; Caballer, A.; Cortese, L.; Vila, C.; Karadeniz, U.; Pagliazzi, M.; Zanoletti, M.; Pacheco, A. P.; Castro, P.; Garcia-de-Acilu, M.; **Mesquita, R. C.***; Busch, D. R.; Durduran, T. HEMOCOVID-19 Consortium

Background: COVID-19 is primarily a respiratory disease; however, there is also evidence that it causes endothelial damage in the microvasculature of several organs. The aim of the present study is to characterize in vivo the microvascular reactivity in peripheral skeletal muscle of severe COVID-19 patients. Methods: This is a prospective observational study carried out in Spain, Mexico and Brazil. Healthy subjects and severe COVID-19 patients admitted to the intermediate respiratory (IRCU) and intensive care units (ICU) due to hypoxemia were studied. Local tissue/blood oxygen saturation (StO(2)) and local hemoglobin concentration (THC) were non-invasively measured on the forearm by near-infrared spectroscopy (NIRS). A vascular occlusion test (VOT), a three-minute induced ischemia, was performed in order to obtain dynamic StO(2) parameters: deoxygenation rate (DeO(2)), reoxygenation rate (ReO2), and hyperemic response (H-AUC). In COVID-19 patients, the severity of ARDS was evaluated by the ratio between peripheral arterial oxygen saturation (SpO(2)) and the fraction of inspired oxygen (FiO(2)) (SF ratio). Results: Healthy controls (32) and COVID-19 patients (73) were studied. Baseline StO(2) and THC did not differ between the two groups. Dynamic VOT-derived parameters were significantly impaired in COVID-19 patients showing lower metabolic rate (DeO(2)) and diminished endothelial reactivity. At enrollment, most COVID-19 patients were receiving invasive mechanical ventilation (MV) (53%) or high-flow nasal cannula support (32%). Patients on MV were also receiving sedative agents (100%) and vasopressors (29%). Baseline StO(2) and DeO(2) negatively correlated with SF ratio, while ReO2 showed a positive correlation with SF ratio. There were significant differences in baseline StO(2) and ReO2 among the different ARDS groups according to SF ratio, but not among different respiratory support therapies. Conclusion: Patients with severe COVID-19 show systemic microcirculatory alterations suggestive of endothelial dysfunction, and these alterations are associated with the severity of ARDS. Further evaluation is needed to determine whether these observations have prognostic implications. These results represent interim findings of the ongoing HEMOCOVID-19 trial.

CRITICAL CARE 25[1], 381, 2021. DOI: 10.1186/s13054-021-03803-2

[P306-2021] "Production of muons from heavy-flavour hadron decays at high transverse momentum in Pb-Pb collisions at ,root S-NN=5.02 and 2.76 TeV"

Acharya, S.; Adamova, D.; Acharya, S.; Adamova, D.; **Albuquerque, D. S. D.*; Chinellato, D. D.*; Takahashi, J.*;** et al. ALICE Collaboration

Measurements of the production of muons from heavy-flavour hadron decays in Pb-Pb collisions at root s(NN) = 5.02 and 2.76 TeV using the ALICE detector at the LHC are reported. The nuclear modification factor R-AA at root s(NN) = 5.02 TeV is measured at forward rapidity (2.5 < y < 4) as a function of transverse momentum p(T) in central, semi-central, and peripheral collisions over a wide p(T) interval, 3 < p(T) < 20 GeV/c, in which muons from beauty-hadron decays are expected to take over from charm as the dominant source at high p(T) (p(T) > 7 GeV/c). The R-AA shows an increase of the suppression of the yields of muons from heavy-flavour hadron decays with increasing centrality. A suppression by a factor of about three is observed in the 10% most central collisions. The R-AA at root s(NN) = 5.02 TeV is similar to that at root s(NN) = 2.76 TeV. The precise R-AA measurements have the potential to distinguish between model predictions implementing different mechanisms of parton energy loss in the high-density medium formed in heavy-ion collisions. They place important constraints for the understanding of the heavy-quark interaction with the hot and dense QCD medium.

PHYSICS LETTERS B 820, 136558, 2021. DOI: 10.1016/j.physletb.2021.136558

[P307-2021] "Quantum Otto engines at relativistic energies"

Myers, N. M.; Abah, O.; **Deffner, S.***

Relativistic quantum systems exhibit unique features not present at lower energies, such as the existence of both particles and antiparticles, and restrictions placed on the system dynamics due to the light cone. In order to understand what impact these relativistic phenomena have on the performance of quantum thermal machines we analyze a quantum Otto engine with a working medium of a relativistic particle in an oscillator potential evolving under Dirac or Klein-Gordon dynamics. We examine both the low-temperature, non-relativistic and high--temperature, relativistic limits of the dynamics and find that the relativistic engine operates with higher work output, but an effectively reduced compression ratio, leading to significantly smaller efficiency than its non-relativistic counterpart. Using the framework of endoreversible thermodynamics we determine the efficiency at maximum power of the relativistic engine, and find it to be equivalent to the Curzon-Ahlborn efficiency.

NEW JOURNAL OF PHYSICS 23[10], 105001, 2021. DOI: 10.1088/1367-2630/ac2756

[P308-2021] "Quantum state truncation using an optical parametric amplifier and a beam splitter"

Mattos, E. P.*; Vidiella-Barranco, A.*

We present a scheme of quantum state truncation in the Fock basis (quantum scissors), based on the combined action of a nondegenerate optical parametric amplifier and a beam splitter. Differently from previously proposed linear--optics-based quantum scissors devices, which depend on reliable Fock state sources, our scheme requires only readily available Gaussian states, such as coherent state inputs (vacuum state included). A truncated state is generated after performing photodetections in the global state. We find that, depending on which output ports each of the two photodetectors is positioned, different types of truncated states may be produced: (i) states having a maximum Fock number of N, or (ii) states having a minimum Fock number N. In order to illustrate our method, we discuss an example having as input states a coherent state in the beam splitter and vacuum states in the amplifier, and show that the resulting truncated states display nonclassical properties, such as subPoissonian statistics and squeezing. We quantify the nonclassicality degree of the generated states using the Wigner-Yanase skew information measure. For complementarity, we discuss the efficiency of the protocol, e.g., generation probability as well as the effects of imperfections such as the detector's quantum efficiency and dark counts rate.

PHYSICAL REVIEW A 104[3], 033715, 2021. DOI: 10.1103/PhysRevA.104.033715

[P309-2021] "Reagentless and sub-minute laser-scribing treatment to produce enhanced disposable electrochemical sensors via additive manufacture"

Rocha, D. P.; Ataide, V. N. **Siervo, A. de***; Gonsalves, J. M.; Munoz, R. A. A.; Paixa, T. R. L. C.; Angnes, L.

3D printing is the most popular form of additive manufacturing, and conductive 3D-printed platforms have been recognized as an emerging class of devices with high potential for electrochemistry. Nevertheless, as-printed electrodes provide poor conductivity due to the presence of high amounts of insulating thermoplastic material, requiring surface post-treatments to enhance their electrochemical performance. Such treatments often employ non-eco-friendly, costly, and time--consuming protocols. In this regard, we propose, for the first time, a sub-minute (around 50 s) and reagentless surface treatment of carbon-black/PLA-based 3D-printed electrodes using a Photo-Thermal approach by a CO2 laser. After the proposed treatment (optimized conditions: the power of 6.2%, the scan rate of 20 mm s-1, and height of 10 mm), a marked improvement in the electrochemical electrode response (current increase and peak-to-peak separation) was achieved towards the detection of catechol, ascorbic and uric acids, paracetamol, hexaammineruthenium(III) chloride, and Ferri/ferrocyanide redox couple. The enhanced simultaneous determination of Cd2+, Pb2+, and Cu2+ was also demonstrated. As a proof--ofconcept, the quantification of the adulterant paracetamol in a real seized cocaine sample was performed using a fully 3D-printed electrochemical system, and a good recovery value of 97.8% was acquired. To explain all the improved results, the electrode was carefully characterized by imaging, spectroscopic and electrochemical techniques. Additionally, the between-measurement % relative standard deviation (%RSD) was 6.8% (n = 12), while the between-device %RSD was 7.5% (n = 6) at the 1 mu mol L-1 paracetamol, indicating adequate manufacturing reproducibility. Thus, the strategies developed here open up new possibilities for applications of carbon--based 3D-printed electrodes in analytical electrochemistry.

CHEMICAL ENGINEERING JOURNAL 425, 130594, 2021. DOI: 10.1016/j.cej.2021.130594

[P310-2021] "Reconfiguration of Amorphous Complex Oxides: A Route to a Broad Range of Assembly Phenomena, Hybrid Materials, and Novel Functionalities"

Prakash, D. J.; Chen, Y. J.; Debasu, M. L.; Savage, D. E.; Tangpatjaroen, C.; **Deneke, C.***; Malachias, A.; Alfieri, A. D.; Elleuch, O.; Lekhal, K.; Szlufarska, I.; Evans, P. G.; Cavallo, F.

Reconfiguration of amorphous complex oxides provides a readily controllable source of stress that can be leveraged in nanoscale assembly to access a broad range of 3D geometries and hybrid materials. An amorphous SrTiO3 layer on a Si:B/Si1-xGex:B heterostructure is reconfigured at the atomic scale upon heating, exhibiting a change in volume of approximate to 2% and accompanying biaxial stress. The Si:B/Si1-xGex:B bilayer is fabricated by molecular beam epitaxy, followed by sputter deposition of SrTiO3 at room temperature. The processes yield a hybrid oxide/semiconductor nanomembrane. Upon release from the substrate, the nanomembrane rolls up and has a curvature determined by the stress in the epitaxially grown Si:B/Si1-xGex:B heterostructure. Heating to 600 degrees C leads to a decrease of the radius of curvature consistent with the development of a large compressive biaxial stress during the reconfiguration of SrTiO3. The control of stresses via post-deposition processing provides a new route to the assembly of complex-oxide-based heterostructures in 3D geometry. The reconfiguration of metastable mechanical stressors enables i) synthesis of various types of strained superlattice structures that cannot be fabricated by direct growth and ii) technologies based on strain engineering of complex oxides via highly scalable lithographic processes and on large-area semiconductor substrates.

SMALL, 2105424, 2021. DOI: 10.1002/smll.202105424

[P311-2021] "Reorganization Energy upon Controlled Intermolecular Charge-Transfer Reactions in Monolithically Integrated Nanodevices"

Merces, L.; Candiotto, G.; Ferro, L. M. M.; Barros, A. de; Batista, C. V. S.; Nawaz, A.; **Riul Jr., A.*;** Capaz, R. B.; Bufon, C. C. B.

Intermolecular electron-transfer reactions are key processes in physics, chemistry, and biology. The electron-transfer rates depend primarily on the system reorganization energy, that is, the energetic cost to rearrange each reactant and its surrounding environment when a charge is transferred. Despite the evident impact of electron-transfer reactions on charge-carrier hopping, well-controlled electronic transport measurements using monolithically integrated electrochemical devices have not successfully measured the reorganization energies to this date. Here, it is shown that self-rolling nanomembrane devices with strain-engineered mechanical properties, on-a-chip monolithic integration, and multi-environment operation features can overcome this challenge. The ongoing advances in nanomembrane-origami technology allow to manufacture the nCap, a nanocapacitor platform, to perform molecular-level charge transport characterization. Thereby, employing nCap, the copper-phthalocyanine (CuPc) reorganization energy is probed, approximate to 0.93 eV, from temperature-dependent measurements of CuPc nanometer-thick films. Supporting the experimental findings, density functional theory calculations provide the atomistic picture of the measured CuPc charge-transfer reaction. The experimental strategy demonstrated here is a consistent route towards determining the reorganization energy of a system formed by molecules monolithically integrated into electrochemical nanodevices.

SMALL 17[45], 2103897, 2021. DOI: 10.1002/smll.202103897

[P312-2021] "Role of resident electrons in the manifestation of a spin polarization memory effect in Mn delta-doped GaAs heterostructures"

Dorokhin, M. V.; Ved, M. V.; Demina, P. B.; Khomitsky, D. V.; Kabaev, K. S.; **Balanta, M. A. G.*; Iikawa, F.***; Zvonkov, B. N.; Dikareva, N. V.

The GaAs/InGaAs quantum wells with a ferromagnetic delta(Mn) layer in GaAs barrier demonstrate a set of interesting spin-related phenomena originating from Mn-hole interaction. One of such phenomena is a spin-memory effect which consists of Mn spin polarization induced by interaction with vicinity spin-polarized holes generated under the exposure by short circularly polarized light pulses. Here long Mn spin relaxation time (similar to 5 ns) allows preserving the spin polarization of the entire system. In the present paper the spin-memory effect investigation was carried out by analyzing the polarization kinetics of quantum-well photoluminescence in the pump-probe technique. It was shown that the photoluminescence circular polarization degree is strongly affected by the magnetic interaction of holes with Mn atoms prepolarized by the pump pulse. In the case of antiparallel Mn and hole polarizations, magnetic interaction leads to decrease of circular polarization degree as compared with single-pulse excitation (so called Delta P effect). Interestingly, the amplitude of hole-mediated Delta P effect is strongly affected by the concentration of resident electrons in the quantum well. The latter was shown to be caused by the specific compliance with selection rules for optical transitions with the participation of unpolarized resident electrons and spin-polarized holes affected by Mn-hole interaction.

PHYSICAL REVIEW B 104[12], 125309, 2021. DOI: 10.1103/PhysRevB.104.125309

[P313-2021] "Search for a heavy Higgs boson decaying into two lighter Higgs bosons in the tau tau bb final state at 13TeV"

Tumasyan, A.; Adam, W.; **Chinellato, J. A.***; et al. CMS Collaboration

A search for a heavy Higgs boson H decaying into the observed Higgs boson h with a mass of 125 GeV and another Higgs boson h(S) is presented. The h and h(S) bosons are required to decay into a pair of tau leptons and a pair of b quarks, respectively. The search uses a sample of proton-proton collisions collected with the CMS detector at a center-of-mass energy of 13TeV, corresponding to an integrated luminosity of 137 fb(-1). Mass ranges of 240-3000 GeV for m(H) and 60-2800 GeV for m(hS) are explored in the search. No signal has been observed. Model independent 95% confidence level upper limits on the product of the production cross section and the branching fractions of the signal process are set with a sensitivity ranging from 125 fb (for m(H) = 240 GeV) to 2.7 fb (for m(H) = 1000 GeV). These limits are compared to maximally allowed products of the production cross section and the branching fractions of the signal process in the next-to-minimal supersymmetric extension of the standard model.

JOURNAL OF HIGH ENERGY PHYSICS [11], 057, 2021. DOI: 10.1007/JHEP11(2021)057

[P314-2021] "Search for chargino-neutralino production in events with Higgs and W bosons using 137 fb(-1) of proton-proton collisions at root s=13 TeV"

Tumasyan, A.; Adam, W.; **Chinellato, J. A.***; et al. CMS Collaboration

A search for electroweak production of supersymmetric (SUSY) particles in final states with one lepton, a Higgs boson decaying to a pair of bottom quarks, and large missing transverse momentum is presented. The search uses data from proton-proton collisions at a center-of-mass energy of 13 TeV collected using the CMS detector at the LHC, corresponding to an integrated luminosity of 137 fb(-1). The observed yields are consistent with backgrounds expected from the standard model.

The results are interpreted in the context of a simplified SUSY model of chargino-neutralino production, with the chargino decaying to a W boson and the lightest SUSY particle (LSP) and the neutralino decaying to a Higgs boson and the LSP. Charginos and neutralinos with masses up to 820 GeV are excluded at 95% confidence level when the LSP mass is small, and LSPs with mass up to 350 GeV are excluded when the masses of the chargino and neutralino are approximately 700 GeV.

JOURNAL OF HIGH ENERGY PHYSICS [10], 045, 2021. DOI: 10.1007/JHEP10(2021)045

[P315-2021] "Search for long-lived particles decaying to jets with displaced vertices in proton-proton collisions at root s=13 Te V"

Tumasyan, A.; Adam, W.; **Chinellato, J. A.***; et al. CMS Collaboration

A search is presented for long-lived particles produced in pairs in proton-proton collisions at the LHC operating at a center--of-mass energy of 13 TeV. The data were collected with the CMS detector during the period from 2015 through 2018, and correspond to a total integrated luminosity of 140 fb(-1). This search targets pairs of long-lived particles with mean proper decay lengths between 0.1 and 100 mm, each of which decays into at least two quarks that hadronize to jets, resulting in a final state with two displaced vertices. No significant excess of events with two displaced vertices is observed. In the context of R-parity violating supersymmetry models, the pair production of long-lived neutralinos, gluinos, and top squarks is excluded at 95% confidence level for cross sections larger than 0.08 fb, masses between 800 and 3000 GeV, and mean proper decay lengths between 1 and 25 mm.

PHYSICAL REVIEW D 104[5], 052011, 2021. DOI: 10.1103/PhysRevD.104.052011

[P316-2021] "Search for W ' bosons decaying to a top and a bottom quark at root s=13 TeV in the hadronic final state"

Tumasyan, A.; Adam, W.; **Chinellato, J. A.***; et al. CMS Collaboration

A search is performed for W' bosons decaying to a top and a bottom quark in the all-hadronic final state, in proton-proton collisions at a center-of-mass energy of 13TeV. The analyzed data were collected by the CMS experiment between 2016 and 2018 and correspond to an integrated luminosity of 137fb(-1). Deep neural network algorithms are used to identify the jet initiated by the bottom quark and the jet containing the decay products of the top quark when the W boson from the top quark decays hadronically. No excess above the estimated standard model background is observed. Upper limits on the production cross sections of W' bosons decaying to a top and a bottom quark are set. Both left- and right-handed W' bosons with masses below 3.4TeV are excluded at 95% confidence level, and the most stringent limits to date on W' bosons decaying to a top and a bottom quark in the all-hadronic final state are obtained.

PHYSICS LETTERS B 820, 136535, 2021. DOI: 10.1016/j.physletb.2021.136535

[P317-2021] "Structural, magnetic and electronic properties of Zn0.94Co0.06O/ZnO heterostructure"

Rajput, P.; Nand, M.; Gupta, M.; Sagdeo, P. R.; Sagdeo, A.; Sharma, S. K.; **Coelho, A. A.***; Jha, S. N.; Bhattacharyya, D.; Kumar, M.

In the present work, single layers of ZnO, Zn0.94Co0.06O and Zn0.94Co0.06O/ZnO heterostructure thin film on quartz substrates as well as on Si (111) substrate have been prepared using RF ion beam sputtering. Grazing incident X-ray diffraction (GIXRD), UV-Vis spectroscopy, X-ray absorption near edge structure (XANES), vibrating sample magnetometer (VSM) and photoelectron spectroscopy (PES) were performed to obtain structural, optical, electronic properties. GIXRD measurement confirms Wurtzite structure of ZnO, whereas UV--Vis spectroscopy shows a blue shift of the absorption edge in Zn0.94Co0.06O single layer with respect to ZnO film with band gap of 3.18 and 3.32 eV for ZnO and Zn0.94Co0.06O single layer films, respectively. The O K-edge spectra revealed O 2p hybridization with Zn3d4s/Co3d states, whereas Co L-3-edge and Co K-edge XANES spectra confirm Co2+ oxidation state. M-H hysteresis measurement at 300 K shows a weak ferromagnetism for Zn0.94Co0.06O single layer and Zn0.94Co0.06O/ZnO heterostructure thin film. Furthermore, to obtain band offset of Zn0.94Co0.06O/ZnO heterostructure thin films, valance band maximum and core level peaks were measured using PES measurement. The offsets in valance band and conduction band for Zn0.94Co0.06O/ZnO heterostructure thin film were obtained as similar to 0.41 eV and similar to 0.55 eV, respectively, and compared with similar to 0.36 eV and similar to 0.51 eV, respectively, of Zn0.9Co0.1O/ZnO heterostructure thin films. The results show that a type-II band alignment in the studied system.

APPLIED PHYSICS A-MATERIALS SCIENCE & PROCESSING 127[11], 827, 2021. DOI: 10.1007/s00339-021-04969-w

[P318-2021] "Study of Z boson plus jets events using variables sensitive to double-parton scattering in pp collisions at 13 TeV"

Tumasyan, A.; Adam, W.; **Chinellato, J. A.***; et al. CMS Collaboration

Double-parton scattering is investigated using events with a Z boson and jets. The Z boson is reconstructed using only the dimuon channel. The measurements are performed with proton-proton collision data recorded by the CMS experiment at the LHC at root s = 13TeV, corresponding to an integrated luminosity of 35.9 fb(-1) collected in the year 2016. Differential cross sections of Z+ >= 1 jet and Z+ >= 2 jets are measured with transverse momentum of the jets above 20 GeV and pseudorapidity vertical bar eta vertical bar < 2.4. Several distributions with sensitivity to double-parton scattering effects are measured as functions of the angle and the transverse momentum imbalance between the Z boson and the jets. The measured distributions are compared with predictions from several event generators with different hadronization models and different parameter settings for multiparton interactions. The measured distributions show a dependence on the hadronization and multiparton interaction simulation parameters, and are important input for future improvements of the simulations.

JOURNAL OF HIGH ENERGY PHYSICS [10], 176, 2021. DOI: 10.1007/JHEP10(2021)176

[P319-2021] "The energy spectrum of cosmic rays beyond the turn-down around 10(17) eV as measured with the surface detector of the Pierre Auger Observatory"

Abreu, P.; Aglietta, M.; **Chinellato, J. A.*; Franco, D. D.*; Dobrigkeit, C.*; Fauth, A. C.*; Payeras, A. M.*; Muller, M. A.*;** et al. Pierre Auger Collaboration

We present a measurement of the cosmic-ray spectrum above 100PeV using the part of the surface detector of the Pierre Auger Observatory that has a spacing of 750 m.

An inflection of the spectrum is observed, confirming the presence of the so-called second-knee feature. The spectrum is then combined with that of the 1500m array to produce a single measurement of the flux, linking this spectral feature with the three additional breaks at the highest energies. The combined spectrum, with an energy scale set calorimetrically via fluorescence telescopes and using a single detector type, results in the most statistically and systematically precise measurement of spectral breaks yet obtained. These measurements are critical for furthering our understanding of the highest energy cosmic rays.

EUROPEAN PHYSICAL JOURNAL C Volume: 81[11], 966, 2021. DOI: 10.1140/epjc/s10052-021-09700-w

[P320-2021] "The mass and galaxy distribution around SZ--selected clusters"

Shin, T.; Jain, B.; **Navarro-Alsina, A.*;** et al.

We present measurements of the radial profiles of the mass and galaxy number density around Sunyaev-Zel'dovich (SZ)--selected clusters using both weak lensing and galaxy counts. The clusters are selected from the Atacama Cosmology Telescope Data Release 5 and the galaxies from the Dark Energy Survey Year 3 data set. With signal-to-noise ratio of 62 (45) for galaxy (weak lensing) profiles over scales of about 0.2-20 h(-1) Mpc, these are the highest precision measurements for SZ-selected clusters to date. Because SZ selection closely approximates mass selection, these measurements enable several tests of theoretical models of the mass and light distribution around clusters. Our main findings are: (1) The splashback feature is detected at a consistent location in both the mass and galaxy profiles and its location is consistent with predictions of cold dark matter N-body simulations. (2) The full mass profile is also consistent with the simulations. (3) The shapes of the galaxy and lensing profiles are remarkably similar for our sample over the entire range of scales, from well inside the cluster halo to the quasilinear regime. We measure the dependence of the profile shapes on the galaxy sample, redshift, and cluster mass. We extend the Diemer & Kravtsov model for the cluster profiles to the linear regime using perturbation theory and show that it provides a good match to the measured profiles. We also compare the measured profiles to predictions of the standard halo model and simulations that include hydrodynamics. Applications of these results to cluster mass estimation, cosmology, and astrophysics are discussed.

MONTHLY NOTICES OF THE ROYAL ASTRONOMICAL SOCIETY 507[4], 5758-5779, 2021. DOI: 10.1093/mnras/stab2505

[P321-2021] "The response of boronized 34CrAlMo5-10 (EN41B) steel to nanoindentation, oxidation, and wear"

Litoria, A. K.; Joshi, M. D.; **Antunes, V.***; Singh, D.; Figueroa, C. A.; **Alvarez, F.***; Hosmani, S. S.

The present study deals with the properties of boronized and non-boronized low-alloy steel (34CrAlMo5-10). Specimens are characterised using microscopy, various spectroscopic techniques, nanoindentation, surface profilometer, and tribometer. The boronized region contains (i) (Fe, M)(2)B columns and (ii) matrix between the columns. Nanoindentation study reveals the difference in the mechanical behaviour of boride, matrix, and core regions. Strain-rate sensitivity of different regions of the specimen cross-section varies between 0.005 and 0.011. The boride phase is more sensitive to the strain-rate than matrix and core. The room-temperature oxidation resistance of the steel surface is enhanced by the presence of a higher proportion of mixed-boride and the oxide layer enriched with Cr2O3. At 550 and 850 degrees C, boronized specimens have higher oxidation resistance than the non-boronized specimens, where the layer of iron-borates protects the surface. At 200 degrees C, the boronized specimen has deprived oxidation resistance. Amongst the investigated wear-parameters, the maximum and minimum wear-resistance of the boronized surface is about 46 and 8 times the wear-resistance of the non--boronized surface, respectively. A steeper drop in the tribological advantage gained by the boronizing treatment is perceived with the increase in load, especially under higher sliding speed.

PHILOSOPHICAL MAGAZINE 101[7], 777-818, 2021. DOI: 10.1080/14786435.2020.1866221

[P322-2021] "The strong CP problem, general covariance, and horizons"

Torrieri, G.*; Truran, H.*

We discuss the strong CP problem in the context of quantum field theory in the presence of horizons. We argue that general covariance places constraints on the topological structure of the theory. In particular, it means that coherence between different topological sectors must have no observable consequence, because the degrees of freedom beyond a causal horizon must be traced over for general covariance to apply. Since the only way for this to occur in QCD is for theta = 0, this might lead to a solution of the strong CP problem without extra observable dynamics.

CLASSICAL AND QUANTUM GRAVITY 38[21], 215002, 2021. DOI: 10.1088/1361-6382/ac27ec

[P323-2021] "Thermodynamics of Statistical Anyons"

Myers, N. M.; **Deffner, S.***

In low-dimensional systems, indistinguishable particles can display statistics that interpolate between bosons and fermions. Signatures of these "anyons" have been detected in two-dimensional quasiparticle excitations of the fractional quantum Hall effect, however experimental access to these quasiparticles remains limited. As an alternative to these "topological anyons," we propose "statistical anyons" realized through a statistical mixture of particles with bosonic and fermionic symmetry. We show that the framework of statistical anyons is equivalent to the generalized exclusion statistics (GES) pioneered by Haldane, significantly broadening the range of systems to which GES apply. We develop the full thermodynamic characterizations of these statistical anyons, including both equilibrium and nonequilibrium behavior. To develop a complete picture, we compare the performance of quantum heat engines with working mediums of statistical anyons and traditional topological anyons, demonstrating the effects of the anyonic phase in both local equilibrium and fully nonequilibrium regimes. In addition, methods of optimizing engine performance through shortcuts to adiabaticity are investigated, using both linear response and fast-forward techniques.

PRX QUANTUM 2[4], 040312, 2021. DOI: 10.1103/PRXQuantum.2.040312

[P324-2021] "Ultrabroadband Nanocavity of Hyperbolic Phonon-Polaritons in 1D-Like alpha-MoO3"

Barcelos, I. D.; Canassa, T. A.; **Mayer, R. A.*; Feres, F. H.***; Oliveira, E. G. de; Goncalves, A. M. B.; Bechtel, H. A.; Freitas, R. O.; Maia, F. C. B.; Alves, D. C. B.

The exploitation of phonon-polaritons in nanostructured materials offers a pathway to manipulate infrared (IR) light for nanophotonic applications. Notably, hyperbolic phonon-polaritons (HP2) in polar bidimensional crystals have been used

to demonstrate strong electromagnetic field confinement, ultraslow group velocities, and long lifetimes (up to similar to 12 ps). Here we present nanobelts of alpha-phase molybdenum trioxide (alpha-MoO3) as a low-dimensional medium supporting HP2 modes in the mid- and far-IR ranges. Through real-space nanoimaging techniques with synchrotron and tunable laser IR light, we observe HP2 FabryPerot resonances that demonstrate distinct anisotropic propagation and frequency dependence. We remark an anisotropic propagation that critically depends on the frequency range. Our findings are supported by the convergence of experiment, theory, and numerical simulations. Our work shows that the low dimensionality of natural nanostructured crystals, like alpha-MoO3 nanobelts, provides an attractive platform to study polaritonic light-matter interactions and offers appealing cavity properties that could be harnessed in future designs of compact nanophotonic devices.

ACS PHOTONICS 8[10], 3017-3026, 172301, 2021. DOI: 10.1021/acsphotonics.1c00955

[P325-2021] "Unusually thick metal-insulator domain walls around the Mott point"

Suarez-Villagran, M. Y.; Mitsakos, N.; Lee, T. H.; Miller, J. H.; **Miranda, E.***; Dobrosavljevic, V.

Many Mott systems feature a first-order metal-insulator transition at finite temperatures, with an associated phase coexistence region displaying inhomogeneities and local phase separation. Here one typically finds "bubbles" or domains of the respective phases, which are separated by surprisingly thick, or fat, domain walls, as revealed both by imaging experiments and recent theoretical modeling. To gain insight into this unexpected behavior, we perform a systematic model study of the structure of such metal-insulator domain walls around the Mott point, within the dynamical mean-field theory framework. Our study reveals that a mechanism producing such "fat" domain walls can be traced to strong magnetic frustration, which is expected to be a robust feature of "spin-liquid" Mott systems.

PHYSICAL REVIEW B 104[15], 155114, 2021. DOI: 10.1103/PhysRevB.104.155114

[P326-2021] "Upsilon production and nuclear modification at forward rapidity in Pb-Pb collisions at root S-NN=5.02 TeV"

Acharya, S.; Adamova, D.; **Albuquerque, D. S. D.*; Chinellato, D. D.*; Takahashi, J.***; et al. ALICE Collaboration

The production of Upsilon mesons in Pb-Pb collisions at a centre-of-mass energy per nucleon pair root S-NN = 5.02 TeV is measured with the muon spectrometer of the ALICE detector at the LHC. The yields as well as the nuclear modification factors are determined in the forward rapidity region 2.5 < y < 4.0, as a function of rapidity, transverse momentum and collision centrality. The results show that the production of the Upsilon(1S) meson is suppressed by a factor of about three with respect to the production in proton-proton collisions. For the first time, a significant signal for the Upsilon(2S) meson is observed at forward rapidity, indicating a suppression stronger by about a factor 2-3 with respect to the ground state. The measurements are compared with transport, hydrodynamic, comover and statistical hadronisation model calculations.

PHYSICS LETTERS B 822, 136579, 2021. DOI: 10.1016/j.physletb.2021.136579

[P327-2021] "Water enabled self-healing polymeric coating with reduced graphene oxide-reinforcement for sensors"

Ly, K. C. S.*; Jimenez, M. J. M.*; Cucatti, S.*; Volpati, D.; Silva, M. A. P. da; **Shimizu, F. M.*; Almeida, T. P.*; Rodrigues, V.***; Silva, J. A. F. da; **Alvarez, F.*; Riul Júnior, A.***

Intrinsic self-healing materials have received significant attention due to the characteristic recovery after damage properties through reversible dynamic covalent and non-covalent interactions. Furthermore, functional recovery with reliable mechanical properties are highly keen as protective coatings, specifically for devices and sensors vulnerable to abrasion in severe environments. Here, we present a functional hierarchical nanostructure capable of multiple micro-sized healings, with enhanced mechanical hardness due to the incorporation of graphene oxide (rGO) nanoplatelets. A self-healing multilayered nanocomposite formed by poly(ethylene imine) (PEI) and poly (acrylic acid) (PAA) was easily assembled by the layer-by-layer (LbL) technique. The addition of the rGO nanoplatelets in the LbL nanostructure resulted in a 13-fold increase in hardness (0.4 +/- 0.1 GPa) when compared to the (PEI/PAA) architecture (0.03 +/- 0.01 GPa). In addition, the nanocomposite presents an enhanced insulating electrical behavior (similar to 4.10(-8) S/cm) despite the addition of the rGO nanoplatelets. Raman and Zeta Potential analysis indicated a possible wrapping of the rGOs by PEI, justifying the observed insulating electrical characteristics. The nanocomposite presents good hydrophobicity with a water contact angle of 136 degrees, interesting to extend the lifetime and protect underlying layers from humidity, degradation, and encrustation. Therefore, we propose an attractive hydrophobic, electrically insulating, and mechanically resistant multifunctional coating for high-performance electronic interfaces from minor cuts and abrasions, dispensing maintainer intervention.

SENSORS AND ACTUATORS REPORTS 3, 100059, 2021. DOI: 10.1016/j.snr.2021.100059

Correções

[Co009-2021] "Measurement of single-diffractive dijet production in proton-proton collisions at root s = 8 TeV with the CMS and TOTEM experiments (vol 80, 1164, 2020)"

Sirunyan, A. M.; Tumasyan, A.; **Chinellato, J. A.*; Manganote, E. J. T.*;** et al.
CMS TOTEM Collaborations; CMS TOTEM Collaborations; TOTEM Collaboration

EUROPEAN PHYSICAL JOURNAL C 81[5], 383, 2021. DOI: 10.1140/epjc/s10052-021-08863-w

***Autores da comunidade IFGW**
Fonte: Web of Science on-line (WOS)

Defesas de Dissertações do IFGW

[D020-2021] "Especiação geográfica no modelo de Manzo--Peliti com genoma finito"
Aluno: Thiago Minetto Pradella
Orientador: Prof. Dr. Marcus Aloísio Martinez de Aguiar
Data: 05/11/2021

Defesas de Teses do IFGW

[T014-2021] "Correlatos neurais da prática de imagética motora com neurofeedback"
Aluno: Carlos Alberto Stefano Filho
Orientador: Profa. Dra. Gabriela Castellano
Data: 27/10/2021

Fonte: Portal IFGW/Pós-graduação - Agenda de Colóquios, Defesas e Seminários.
Disponível em: http://portal.ifi.unicamp.br/pos-graduacao

Defesas de Teses e Dissertações do PECIM

Observação: Não ocorreram neste período defesas de teses e dissertações, com orientadores ou banca do IFGW, do Programa de Pós-Graduação Multiunidades em Ensino de Ciências e Matemática – Mestrado e Doutorado (PECIM) da Unicamp.

Fonte: Página do PECIM
Disponível em: https://www.pecim.unicamp.br/bancas

A BIF deseja a todos um Natal de muita paz e harmonia e um 2022 repleto de sonhos e esperanças renovadas!

Abstracta

Instituto de Física "Gleb Wataghin" - IFGW
Diretora: Profa. Dra. Mônica Alonso Cotta
Diretor Associado: Prof. Dr. Marcos Cesar de Oliveira
Universidade Estadual de Campinas - UNICAMP
Cidade Universitária Zeferino Vaz
13083-859 - Campinas - SP - Brasil
e-mail: secdir@ifi.unicamp.br
Fone: +55 19 3521-5300

Publicação

Biblioteca do Instituto de Física Gleb Wataghin
http://portal.ifi.unicamp.br/biblioteca

Diretora Técnica: Sandra Maria Carlos Cartaxo
Coordenadora da Comissão de Biblioteca: Profa. Dra. Arlene Cristina Aguilar

Elaboração:
Maria Graciele Trevisan (Bibliotecária)
contato: infobif@ifi.unicamp.br